A Model-Based Diagnostic Study of the Rapid Development Phase of the Presidents' Day Cyclone

JEFFREY S. WHITAKER,* LOUIS W. UCCELLINI[†] AND KEITH F. BRILL[†,‡]

*Department of Meteorology, The Florida State University, Tallahassee, Florida
[†]Laboratory for Atmospheres, NASA/Goddard Space Flight Center, Greenbelt, Maryland
[‡]General Sciences Corporation, Laurel, Maryland

ABSTRACT

A model simulation of the rapid development phase of the Presidents' Day cyclone of 19 February 1979 is analyzed in an effort to complement and extend a diagnostic analysis based only on 12-h radiosonde data over the contiguous United States, with a large data-void area over the Atlantic Ocean (Uccellini et al. 1985). As indicated by the SLP and 850 mb absolute vorticity tendencies, rapid cyclogenesis commences between 0300 and 0600 UTC 19 February and proceeds through the remaining 18 h of the simulation. This rapid development phase occurs as stratospheric air [marked by high values of potential vorticity (PV)] approaches and subsequently overlies a separate, lower-tropospheric PV maximum confined to the East Coast, or during the period when the advection of PV increases in the middle to upper troposphere over the East Coast. The onset of rapid deepening is marked by 1) the transition in the mass divergence profiles over the surface low from a diffuse pattern with two or three divergence maxima to a two-layer structure, with maximum divergence located near 500 mb and the level of nondivergence located near 700 mb; 2) the intensification of precipitation just north of the surface low pressure system; and 3) an abrupt increase in the low-level vorticity.

Model trajectories and Eulerian analyses indicate that three airstreams converge into the cyclogenetic region during the rapid development phase. One of these airstreams descends within a tropopause fold on the west side of an upper-level trough over the north-central United States on 18 February and approaches the cyclone from the west-southwest as the rapid development commences. A second airstream originates in a region of lower-tropospheric subsidence within the cold anticyclone north of the storm, follows an anticyclonically curved path at low levels over the ocean, and then ascends as it enters the storm from the east. A third airstream approaches the storm from the south at low levels and also ascends as it enters the storm circulation. All of the airstreams pass through the low-level PV maximum as they approach the storm system, with the PV increase following a parcel related to the vertical distribution of θ due to the release of latent heat near the coastal region.

A vorticity analysis shows that absolute vorticity associated with the simulated storm is realized primarily through vortex stretching associated with the convergence of the airstreams below the 700 mb level. Although the maximum vorticity is initially confined below the 700 mb level, the convergence of the various airstreams is shown to be directly related to dynamic and physical processes that extend throughout the entire troposphere. Finally, the divergence of these airstreams within the 700 to 500 mb layer increases the magnitude of the mass divergence just north and east of the storm center and thus enhances the rapid deepening of the surface low as measured by the decreasing sea level pressure.

1. Introduction

On 18–19 February 1979, a very intense cyclone developed along the Middle Atlantic coast, producing heavy snow and high winds from North Carolina to southeastern New York and extreme southern New England. This storm, known as the Presidents' Day storm, is a classic case of a rapidly developing coastal cyclone and is of particular interest because of its rapid intensification and heavy snowfall, which were poorly forecast by operational models.

Corresponding author address: Dr. Louis W. Uccellini, Severe Storms Branch, Laboratory for Atmospheres, NASA/Goddard Space Flight Center, Code 612, Greenbelt, MD 20771.

Observation-based studies of the Presidents' Day cyclone have identified two separate phases of storm development, each associated with a distinct area of heavy snowfall: 1) the initial development of a coastal front and inverted trough off the Carolina coast on 18 February, and 2) the rapid development of the cyclone along the Middle Atlantic coast on 19 February which produced the heavy snow from Washington, D.C., to New York City. The importance of an advancing mid-tropospheric short-wave trough on the rapid development phase on 19 February was explored by Bosart (1981), Bosart and Lin (1984), and Uccellini et al. (1985). The diagnostic analyses by Uccellini et al. (1985) established a relationship between tropopause folding associated with frontogenesis in the middle to upper troposphere accompanying an amplifying polar

jet (PJ)-trough system on 18 February and the subsequent rapid cyclogenesis on 19 February. These results demonstrated that dry stratospheric air marked by high values of potential vorticity (PV) was extruded downward within a tropopause fold 1500 km upstream of the East Coast and 12 to 24 h *prior* to cyclogenesis. During the 12 h preceding rapid cyclogenesis, the stratospheric air descended toward the 800 mb level, approached another source of high PV air near the coastal front and inverted trough, and was nearly collocated with the storm center during the period of rapid cyclogenesis.

Due to the poor temporal resolution of the radiosonde data base and the data-void region off the Middle Atlantic coast, no attempt could be made in the observational studies cited above to diagnose the apparent interaction of the stratospheric air mass and the developing cyclone, nor to assess the relative contributions of vertical stretching and tilting effects to the rapid increase in cyclonic vorticity after 1200 UTC 19 February. Keyser and Uccellini (1987) review the successful application of regional- and mesoscale model simulations in providing high-resolution and dynamically consistent data required for diagnostic studies which are designed to resolve mesoscale processes associated with significant weather events. In a recent model-based study, Uccellini et al. (1987) utilize a series of numerical simulations to resolve the interaction between dynamic and thermodynamic processes that contribute to the *initial development phase* of the Presidents' Day cyclone on 18 February 1979. In the present study, a regional-scale model simulation is used to alleviate the shortcomings of the observation-based studies cited earlier and to examine the interaction of various physical processes during the *rapid development phase* of the Presidents' Day cyclone on 19 February.

The specific purposes of this paper are 1) to present a model simulation of the Presidents' Day cyclone initialized at 1200 UTC 18 February that captures the upper-tropospheric intrusion of stratospheric air (marked by high PV values) on 18 February; 2) to use the model simulation to examine the descent of the stratospheric air mass identified by Uccellini et al. (1985) and, more importantly, the interaction of this air mass with a lower-tropospheric PV maximum associated with the inverted trough and coastal front that could not be resolved using the operational data base; and 3) to examine the processes that contribute to the rapid decrease of sea level pressure and simultaneous rapid increase in lower-tropospheric cyclonic vorticity.

A brief synoptic overview of the Presidents' Day cyclone is presented in section 2. Section 3 provides a brief description of the numerical model and the initial conditions for the model simulation. In section 4, the evolution of the PJ-trough system and its associated tropopause fold is described, along with the simulated surface low and the vertical profile of mass divergence which contributes to the decreasing sea-level pressure.

An evaluation of the various terms in the vorticity equation is presented in section 5 to identify the processes contributing to the increase in absolute vorticity. In section 6, diagnostics from a Lagrangian perspective are used to clarify the nature and origin of airstreams entering the low-level circulation associated with the rapid cyclogenesis. The results of the study and remaining issues are summarized in section 7.

2. Synoptic overview

By 12Z/18,[1] snow and sleet were occurring in the southern United States within an inverted surface trough extending northward from the Gulf of Mexico (Fig. 1a). At the same time, a separate trough was beginning to develop off the Southeast Coast in response to increased divergence along the axis of an amplifying subtropical jet (STJ) over the carolinas and the development of a coastal front (Uccellini et al. 1987). By 00Z/19, weak surface lows formed along the coastal front-inverted trough off the Georgia coast and within the northern portion of an inverted trough in the Ohio Valley (Fig. 1b). Heavy snow continued along the East Coast, while moderate snow developed in the Ohio Valley. By 12Z/19, the weak surface low over the Ohio Valley had disappeared as rapid cyclogenesis was in progress along the East Coast (Fig. 1c). The coastal system then moved slowly east over the Atlantic Ocean and developed into an intense vortex with hurricane-force winds (Fig. 1d). Based on the observational studies cited above, the rapid development phase of the storm is generally considered to have commenced at approximately 06Z/19, and continued during the following 12 to 18 h.

Aloft, the surface cyclogenesis on 19 February appears to be linked with the arrival of the polar jet/trough system which propagated from the central United States at 12Z/18 (Fig. 2a) to the East Coast by 12Z/19 (Fig. 2c). Bosart and Lin's (1984) analysis of the semigeostrophic PV and studies by Uccellini et al. (1984, 1985) indicate that the PJ-trough system was exerting a significant influence on the surface cyclogenesis by 12Z/19. At 00Z/19, this trough and associated PJ (with wind speeds exceeding 50 m s^{-1}) were located over the Ohio Valley (Fig. 2b), poised to the west of the cyclogenetic region. A vertical cross section along the solid line in Fig. 2b depicts the PJ centered near 300 mb and a STJ core near 200 mb (Fig. 3) at 00Z/19. Stratospheric air was descending into the middle and lower troposphere within a tropopause fold over the central United States as the amplifying PJ-trough system propagated toward the Ohio Valley. The PJ-trough system and descending stratospheric air mass

---

[1] The time and date format used in this paper is consistent with other Presidents' Day storm papers (i.e., 1200 UTC 19 February is abbreviated 12Z/19).
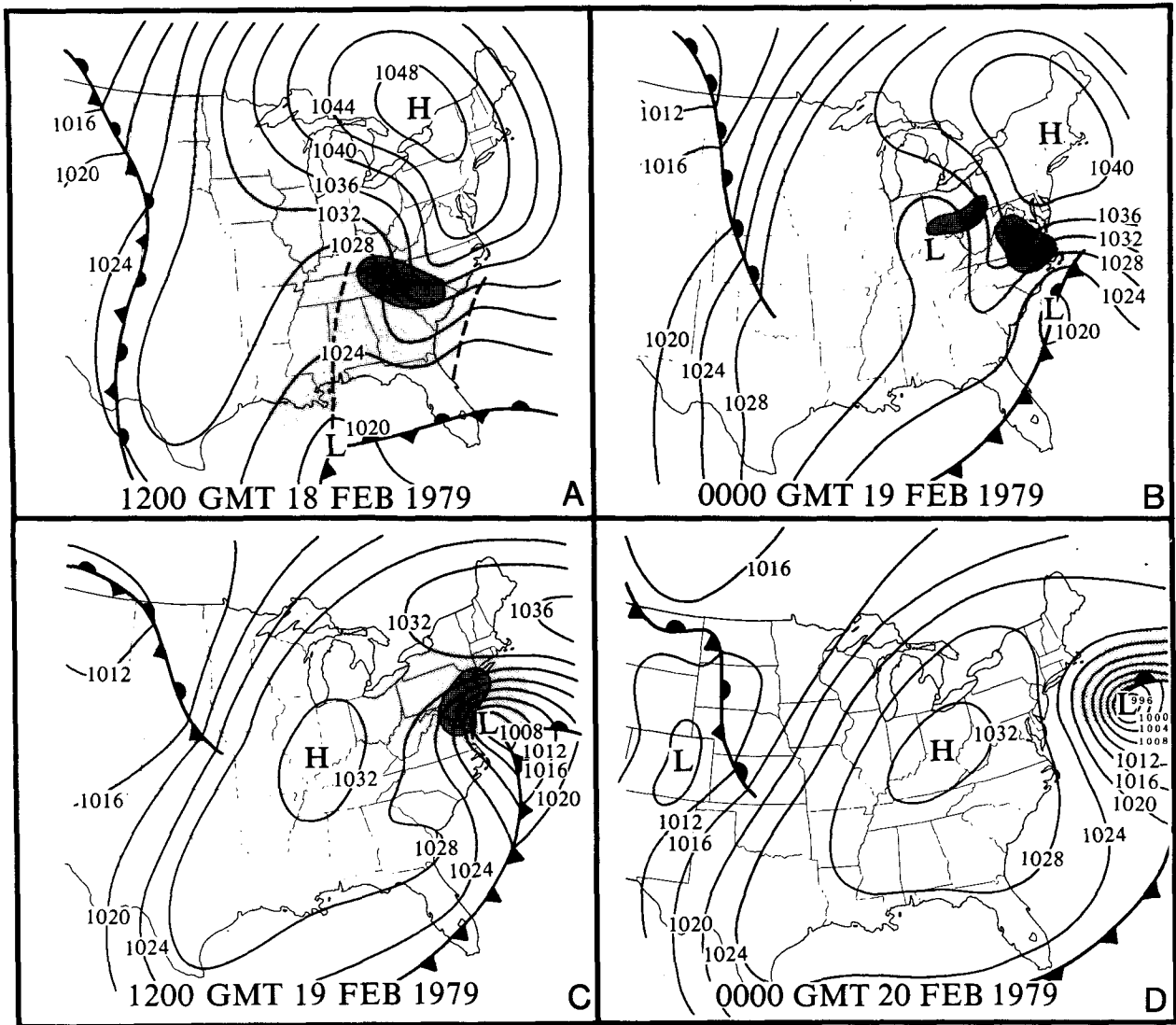
FIG. 1. Sea-level pressure (mb) and surface frontal analyses for (a) 1200 UTC 18 February, (b) 0000 UTC 19 February, (c) 1200 UTC 19 February, and (d) 0000 UTC 20 February. Shading indicates precipitation, and dark shading indicates moderate to heavy precipitation. Dashed lines in (a) denote inverted and coastal troughs [from Uccellini et al. (1984)].

reached the East Coast by 12Z/19, coinciding with the onset of rapid cyclogenesis.

A unique aspect of the Uccellini et al. (1985) study is the emphasis on the descent of the tropopause fold to the middle troposphere *prior* to cyclogenesis and 1500 to 2000 km upstream of the East Coast. This emphasis is in contrast to other studies cited by Uccellini et al. (1985, pp. 980–981) that describe the descent of the tropopause fold toward the middle troposphere as occurring *during* the cyclogenetic period. However, the lack of data immediately off the East Coast prevents any analyses of the interaction of the stratospheric air mass with the rapidly developing storm which occurred primarily over the ocean. In the following sections, diagnostics from a mesoscale model simulation are pre-

sented to provide insight into this and other physical processes that contributed to the rapid cyclogenesis over the western Atlantic Ocean for this case.

3. The numerical model and initial conditions

The numerical model used in this study is an updated version of the Mesoscale Analysis and Simulation System (MASS), a diabatic, hydrostatic primitive equation model developed by Kaplan et al. (1982) and evaluated by Koch et al. (1985). As discussed by Uccellini et al. (1987), several modifications have been made, including 1) an improved boundary layer parameterization based on the separate treatment of free convection over land (Businger 1973) and water (Stage
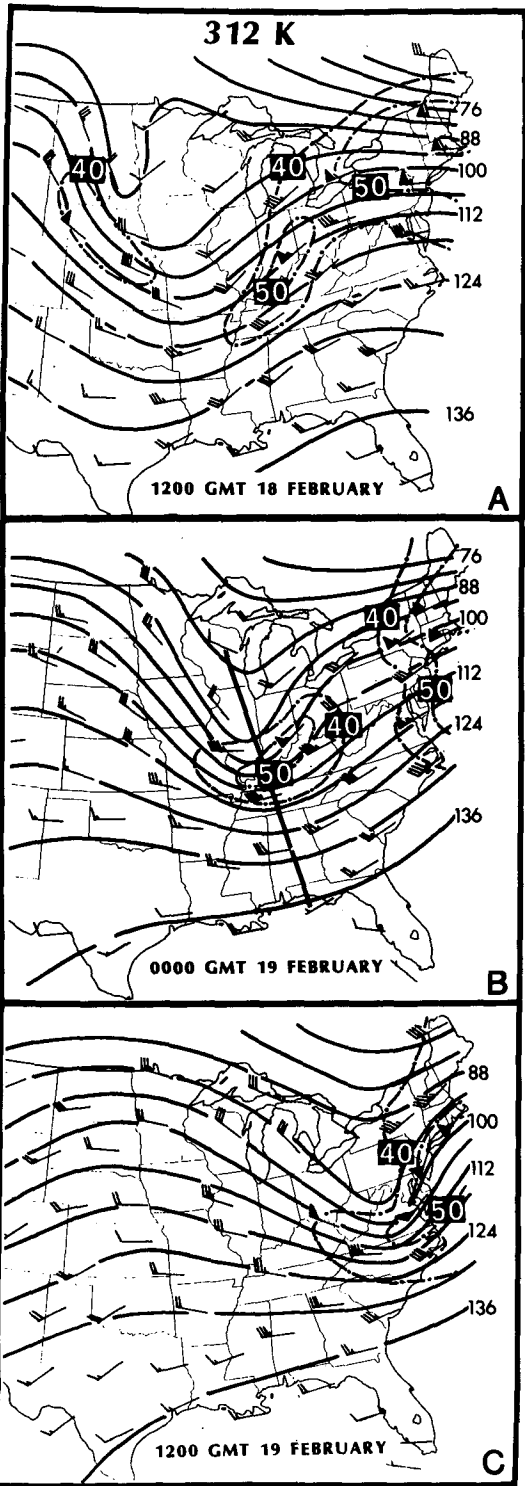
FIG. 2. The 312 K analyses of Montgomery streamfunction (solid, $124 = 3.124 \times 10^5$ m^2 s^{-2}) and isotachs (dot-dash, m s^{-1}) for (a) 1200 UTC 18 February, (b) 0000 UTC 19 February, and (c) 1200 UTC 19 February. Wind barbs represent observed wind speeds (solid triangular barbs denote 50 m s^{-1}, whole barbs 10 m s^{-1}, and half barbs 5 m s^{-1}). Solid line in (b) indicates position of cross section in Fig. 3 [from Uccellini et al. (1985)].
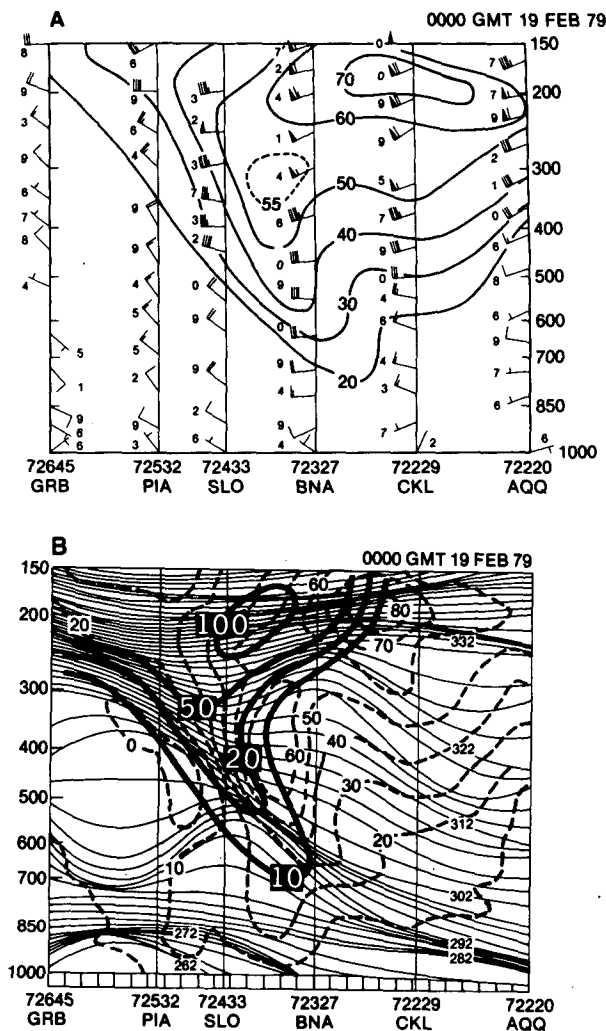

FIG. 3. Vertical cross section from Green Bay, Wisconsin (GRB), to Apalachicola, Florida (AQQ), for 0000 UTC 19 February 1979. (a) Isotach analysis for total wind speed (solid, m s^{-1}), wind barbs plotted as in Fig. 2 with last digit of observation. (b) Isentropes (solid, K), geostrophic wind speed normal to plane of cross section (dashed, m s^{-1}), and potential vorticity (thick solid where $10 = 10 \times 10^{-6}$ K mb^{-1} s^{-1}) [from Uccellini et al. (1985)].

and Businger 1981) and 2) the addition of the Molinari (1982) cumulus scheme.

The simulation performed for this study was run on a 128 × 96 horizontal array of grid points separated by a constant distance of 58.5 km on the polar stereographic map image plane. Thirty-two equally spaced vertical sigma levels between the surface and 100 mb were specified in order to develop and maintain structure in the tropopause fold. The lateral boundary conditions utilize time tendencies of the dependent variables obtained from the European Centre for Medium Range Weather Forecasts (ECMWF) mandatory-level First Global GARP Experiment (FGGE) analyses. The model was initialized at 12Z/18 using an isentropic

insert technique, a variational adjustment of temperature under hydrostatic constraints, and a final adjustment to the wind field to minimize the integrated mass divergence as described by Uccellini et al. (1987).

The initial analysis used in this model simulation (Fig. 4) depicts the following precyclogenetic features discussed in section 2: 1) the polar jet over the north-central Plains with wind speeds exceeding 40 m s^{-1} (Fig. 4a); 2) the inverted sea-level pressure trough extending northward from the Gulf of Mexico and the strong surface ridge along the East Coast reflecting the damming of cold air along the east side of the Appalachians (Fig. 4b); and 3) the moderate temperature gradient off the Southeast Coast that marks the onset of coastal frontogenesis (Fig. 4b). The sea-surface temperature analysis is derived from the monthly mean climatological values and is shown in Fig. 4c.

4. Model simulation

In this section, the basic structure of the simulated storm is discussed. Isentropic maps and cross sections are then presented to describe: 1) the eastward propagation and downward extrusion of stratospheric air marked by high PV values within the upper-tropospheric frontal zone and 2) the subsequent interaction of this stratospheric air mass with a low-level PV maximum associated with the developing coastal front and inverted trough along the Middle Atlantic coast.

a. Simulation of the storm

During the first 6 h of the model simulation (by 18Z/18), an inverted trough is developing off the Southeast Coast accompanied by coastal frontogenesis, which is represented by the strengthening in the temperature gradients along the South Carolina coastal plain (Fig. 5a). The inverted trough extending northward from the Gulf of Mexico into the Ohio Valley still exists (not shown), but the heaviest precipitation is developing in association with the developing coastal system. By 12 h (00Z/19), the coastal trough develops into a closed cyclonic circulation with a central pressure of 1019 mb (Fig. 5b), which compares to an observed central pressure of 1018 mb (Bosart 1981). Heavy precipitation is concentrated along the Virginia–North Carolina coast, with a small area of moderate to heavy precipitation also developing over northern Virginia between 03Z/19 and 06Z/19. The low deepens to 1013 mb by 06Z/19 while moving northward to a position over the North Carolina coast (Fig. 5c). The coastal front continues to strengthen and extends northward into the Chesapeake Bay region by this time. The central pressure drops 8 mb over the next 6 h, reaching 1005 mb at 12Z/19 [compared to 1006 mb in Bosart's (1981) analysis], while the storm moves to a position near the mouth of the Chesapeake Bay and the precipitation shield continues to spread north and east of the developing surface low (Fig. 5d).
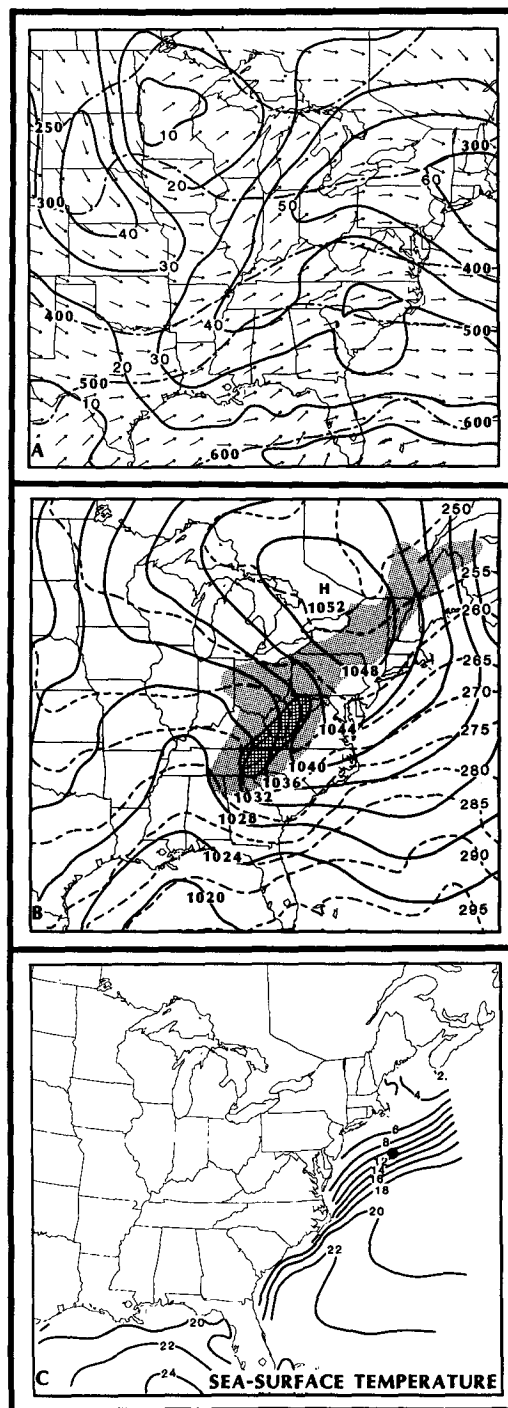

FIG. 4. Initial fields for the model simulation at 1200 UTC 18 February: (a) isotachs (solid, m s^{-1}), pressure (dot-dashed, mb), and arrows to denote wind direction for the 312 K surface; (b) sea-level pressure (solid, mb) and temperature at the midpoint of the lowest model layer (dashed, K); and (c) sea-surface temperature (°C). The midpoint of the lowest model layer ($\sigma = 0.9844$) is about 29 mb above the surface. Light shading indicates terrain heights of 250 to 500 m, and dark shading indicates terrain heights of greater than 500 m above sea level. The black circle in (c) indicates a buoy at 39°N, 70°W.
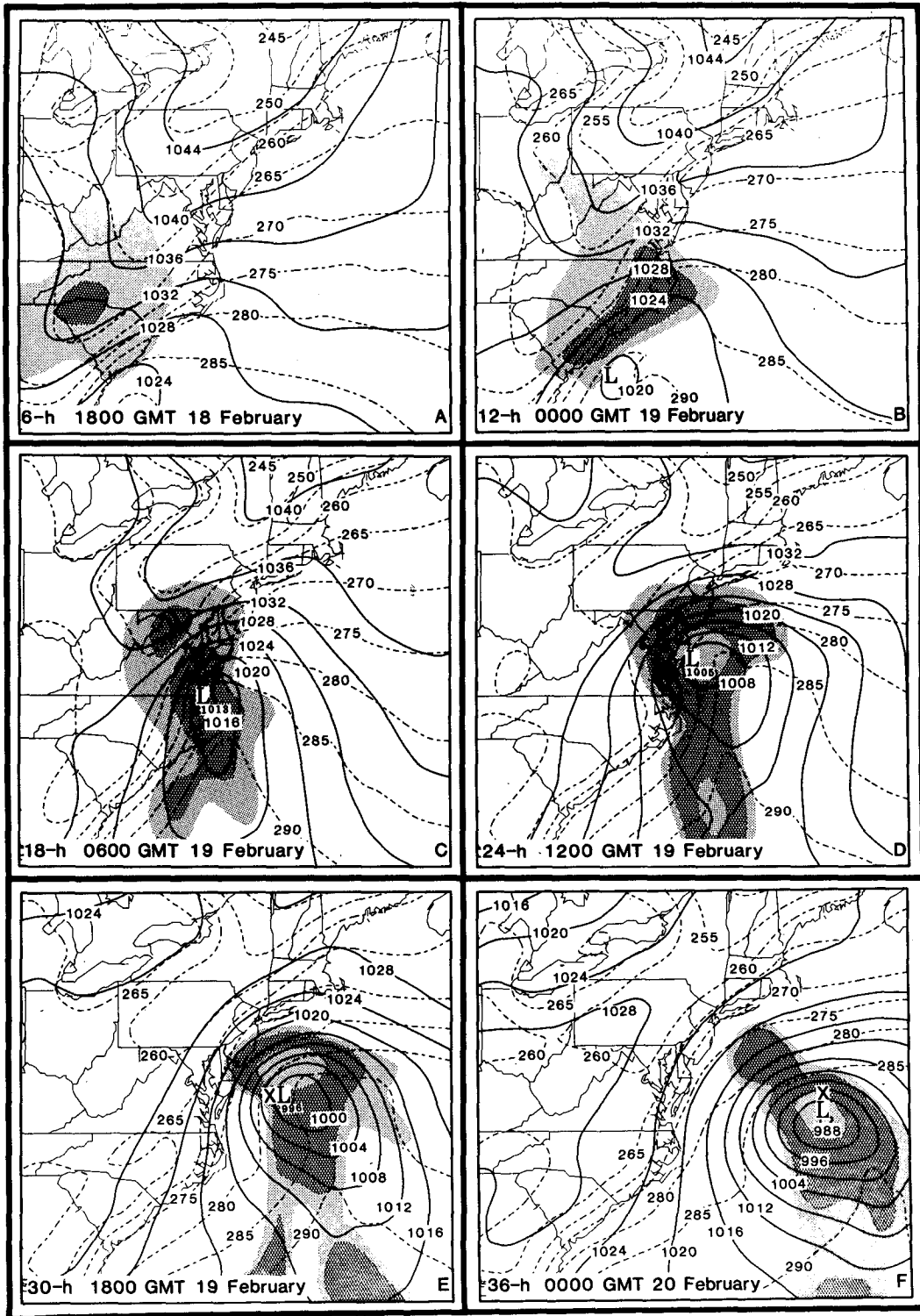
FIG. 5. Sea-level pressure (solid, mb) and temperature at the midpoint of the lowest model layer (dashed, K) from the model simulation at (a) 6 h (1800 UTC 18 February), (b) 12 h (0000 UTC 19 February), (c) 18 h (0600 UTC 19 February), (d) 24 h (1200 UTC 19 February), (e) 30 h (1800 UTC 19 February), and (f) 36 h (0000 UTC 20 February). Light shading indicates 6-h accumulated precipitation of 0.025 to 1 cm, dark shading greater than 1 cm, and the inner areas of light shading greater than 4 cm during the 6 h ending at the time indicated on each panel. The X's in (e) and (f) represent observed positions of the surface low.
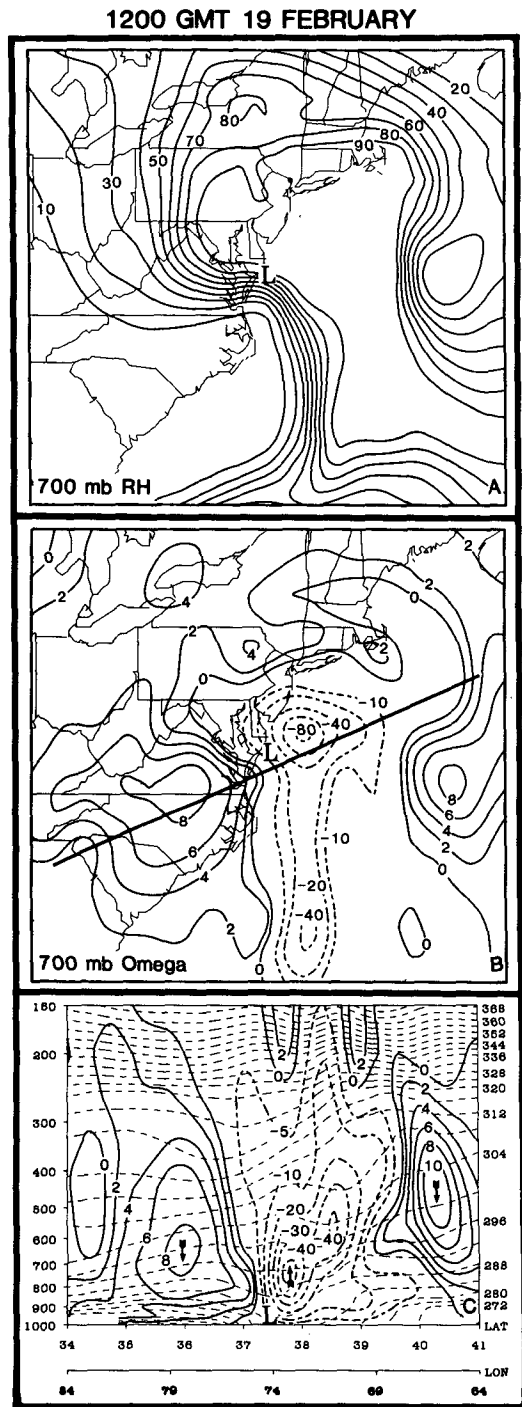
1200 GMT 19 FEBRUARY

FIG. 6. The 700 mb analyses of (a) relative humidity (percent) and (b) omega (μb s^{-1}) at 24 h (1200 UTC 19 February); (c) is a cross section of potential temperature (dashed, K) and omega [solid-positive, dashed-negative (μb s^{-1})] along solid line in (b). Note: contour intervals for negative contours in (c) are irregular for legibility.

Analyses of 700 mb relative humidity (RH) and isobaric vertical motion (ω) (Figs. 6a and 6b) at 12Z/19 illustrate an intrusion of dry, subsiding air into the southwestern quadrant of the storm and the ascending, moist air to the north and east of the storm system, with the cyclone centered in the moisture gradient between the two regions. This is consistent with the satellite cloud and moisture imagery described by Uccellini et al. (1985). The cross section in Fig. 6c depicts the deep layer of subsidence on the cold side of the storm, and the strong ascent to the north and east of the low center at this time. The ω pattern replicates the well-known distribution of vertical motion associated with rapidly developing extratropical cyclones (e.g., Krishnamurti 1968). Furthermore, the magnitude of the ascent maximum is consistent with values expected over small domains during rapid oceanic cyclogenesis [see, e.g., Shapiro et al. (1987)]. However, an important, unresolved issue remains concerning the means by which the simulated latent heat release (due to grid-resolvable and subgrid-scale precipitation processes simulated by the regional-scale model) affects the magnitude of ω and the deepening rate of the cyclone. This problem has been recognized for this and other modeling systems (e.g., Anthes and Keyser 1979; Koch et al. 1985) and is discussed further in section 7.

After 12Z/29, the storm takes a more easterly track, deepening 9 mb to 996 mb between 12Z/19 and 18Z/19 (Fig. 5e) and 8 mb to 988 mb between 18Z/19 and 00Z/20 (Fig. 5f). Comparisons with observations are difficult for this portion of the model simulation, given the absence of ship reports near the storm center (Bosart 1981, p. 1555) and the difference in the analyses provided by NMC and Bosart (1981). Bosart's estimated central pressure of 990 mb at 18Z/19 compares with NMC's analyzed central pressure of 996 mb at 18Z/19 and 995 mb at 00Z/20. The simulation produces a more rapid deepening than that analyzed by NMC, but not quite as rapid as that estimated by Bosart. Nevertheless, between 12Z/19 and 00Z/20, the tracks of ths simulated and observed cyclones are very close, with the model storm track deviating from the observed storm track by less than 110 km (see Figs. 5e and 5f).

The model SLP fields in Fig. 5 indicate a continued deepening of the simulated storm system during the entire 36-h period, with an enhancement of the deepening rate occurring sometime between 00Z/19 and 06Z/19. A comparison between observed SLP traces from coastal stations and those produced by the model (not shown) indicates that the period of rapid deepening (as measured by the SLP) commenced between 03Z/19 and 06Z/19. Analyses of the SLP tendencies and mass divergence profiles illustrate that a transition throughout the troposphere accompanies the onset of enhanced deepening of the simulated storm. The mass divergence in σ coordinates is related to the surface pressure tendency through the equation

$$\frac{\partial p_s}{\partial t} = \int_{\sigma=1}^{\sigma=0} \nabla_\sigma \cdot \left(\frac{\partial p}{\partial \sigma} \mathbf{V}\right) d\sigma, \tag{1}$$
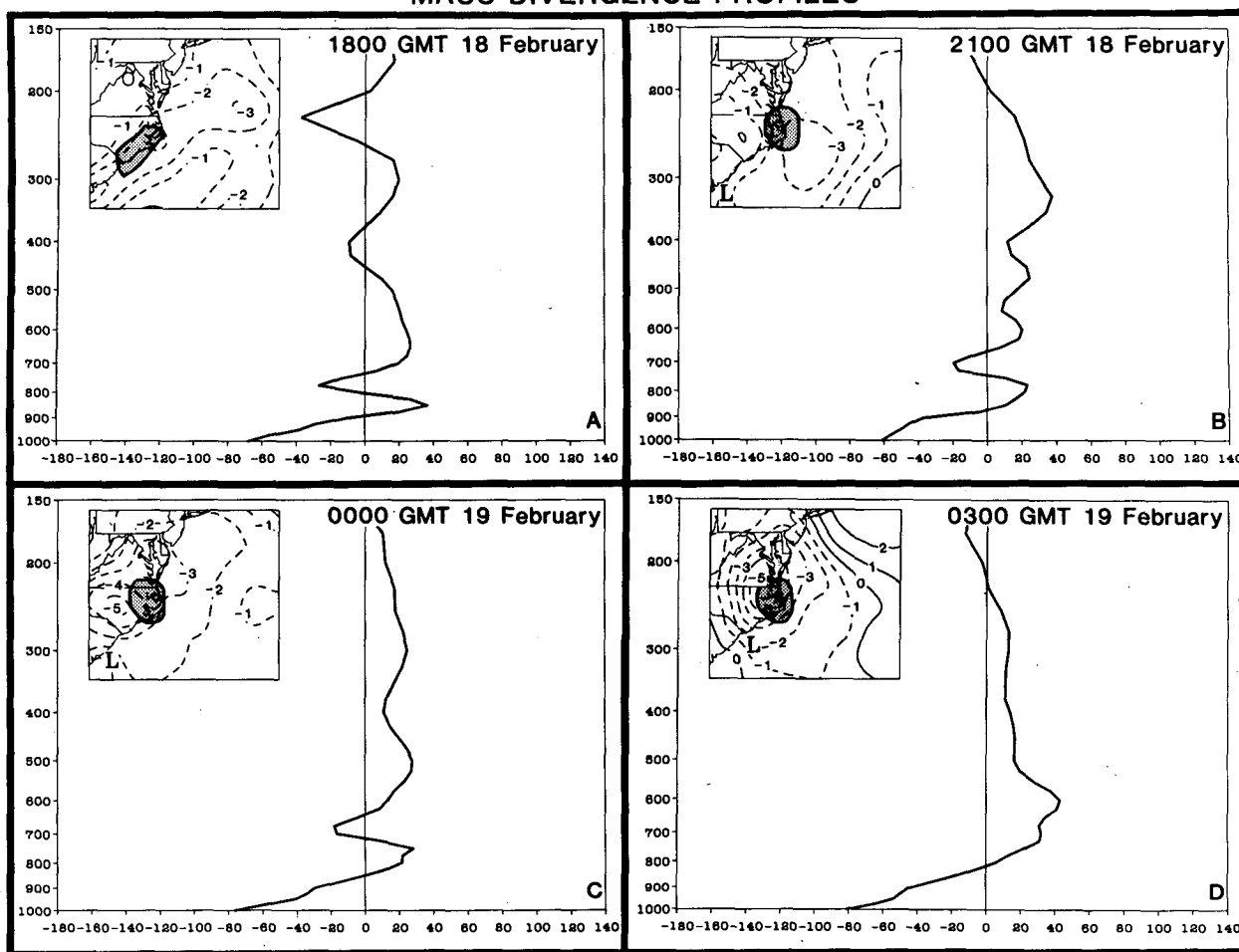
MASS DIVERGENCE PROFILES

FIG. 7. Area-averaged vertical profiles of mass divergence ($10 = 10 \times 10^{-3}$ mb s^{-1}) computed for (a) 6 h (1800 UTC 18 February), (b) 9 h (2100 UTC 18 February), (c) 12 h (0000 UTC 19 February), (d) 15 h (0300 UTC 19 February), (e) 18 h (0600 UTC 19 February), (f) 21 h (0900 UTC 19 February), (g) 24 h (1200 UTC 19 February), and (h) 27 h (1500 UTC 19 February) before and during the rapid deepening phase. The profiles are computed for shaded regions depicted on map inset for each time. The 3-h pressure changes (mb) and locations of the surface low center are depicted on each map inset.

where $\partial p/\partial \sigma$ is a measure of the mass between σ surfaces and V is the two-dimensional horizontal wind velocity. The 3-h pressure tendencies and vertical profiles of the mass flux divergence are depicted in Fig. 7 for the 3-h time increments between 18Z/18 and 15Z/19. The mass divergence is averaged over 30 grid points represented by the shaded area in each map inset.

At 18Z/18 (Fig. 7a), 21Z/18 (Fig. 7b), and 00Z/19 (Fig. 7c), the mass divergence contributing to the decreasing SLP is maximized in two distinct layers. One is located near 875 mb at 18Z/18, rising to 775 mb by 00Z/19 in association with the entrance region of the low-level jet (LLJ) (Uccellini et al. 1987). The second mass divergence maximum is located above the 700 mb level at 18Z/18 (Fig. 7a) and becomes organized as one layer of divergence between 650 and 175 mb by 00Z/19 (Fig. 7c), although this mass divergence

maximum remains between 20 to 40 ($\times 10^{-3}$) mb s^{-1}. The upper-level mass divergence was found by Uccellini et al. (1987) to coexist with the axis of a STJ extending west-to-east across the Carolina coast during this period.

Between 00Z/19 and 03Z/19, a transition commences in the mass divergence profiles. The mass convergence in the low levels extends over a deeper layer in conjunction with the developing cyclone (Fig. 5c). At the same time, a single (yet broadly defined) maximum in the mass divergence becomes established near 600 mb, with a level of nondivergence located near the 800 mb level. The maxima of the upper-level mass divergence and lower-level mass convergence both increase in magnitude and become better defined after 03Z/19 (Figs. 7d–7h), with the level of nondivergence rising slowly to the 700 mb level during this period.
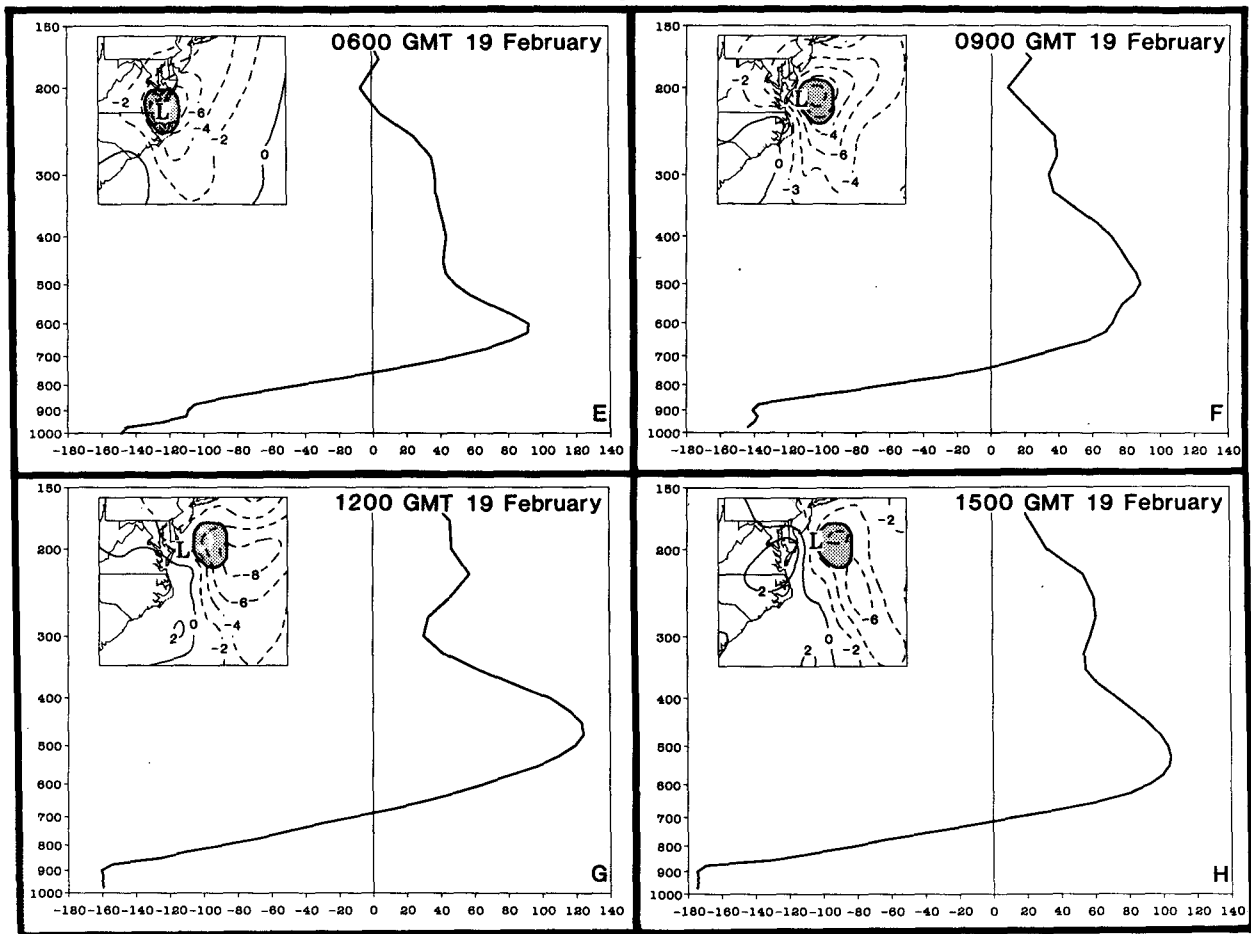
MASS DIVERGENCE PROFILES

FIG. 7. (Continued)

The two-layer structure for the divergence field is similar to the schematic profiles deduced for extratropical cyclones by Bjerknes and Holmboe (1944). Furthermore, the amplification in the mass divergence (convergence) in the upper (lower) troposphere coincides with 1) a significant increase in the precipitation rates (Fig. 5 and Table 1), a result that agrees with the budget study of a midwestern cyclone conducted by Johnson and Downey (1975), and 2) the approach and eventual arrival of the PJ-trough system from the west, as described below.

b. Simulation of the PJ-trough system and associated tropopause fold upstream and prior to rapid cyclogenesis

Since Kleinschmidt's assertion that the stratospheric reservoir of PV "is essentially the producing mass of cyclones" (Eliassen and Kleinschmidt 1957, p. 125), a growing number of papers have provided evidence for

the influence of stratospheric extrusions in surface cyclogenesis [e.g., see Danielsen (1968), Bleck (1973), Bleck and Mattocks (1984), Uccellini et al. (1985), Hoskins et al. (1985), Boyle and Bosart (1986)]. Isentropic maps and vertical cross sections derived from the model data are now presented to provide further insight into the time evolution and structure of the PJ-trough system and associated tropopause fold and its subsequent influence on the Presidents' Day cyclone along the East Coast.[2]

At the initial time, the PJ on the 312 K surface is located near the inflection point on the west side of the trough over the middle of the United States, with maximum wind speeds exceeding 45 m s^{-1} (Fig. 4a). Although large values of PV [defined by the expression

---

[2] All diagnostic and predicted quantities presented in this paper were interpolated horizontally from the model domain to a 0.5° latitude–longitude grid by overlapping quadratic polynomials and vertically by linear variation in σ to isentropic surfaces at 4 K increments and pressure surfaces at 50 mb increments.

TABLE 1. Listing of the sea-level pressure (SLP) minimum and pressure tendency at the center of the simulated cyclone, the 3-h grid-resolvable precipitation (centimeters) averaged for the areas used to compute mass divergence profiles in Fig. 7, and the 850 mb absolute vorticity maximum.

	18 February				19 February								
	12Z	15Z	18Z	21Z	00Z	03Z	06Z	09Z	12Z	15Z	18Z	21Z	00Z
SLP min (mb)	1029	1026	1023	1021	1019	1018	1013	1007	1005	1002	996	992	988
6-h tendency (mb)	←──── −6 ──→←── −4 ──→←── −6 ──→←── −8 ──→←── −9 ──→←── −8 ──→												
Averaged precipitation (cm)			.2	.7	.5	.4	1.0	1.5	2.8	2.4			
850 mb vorticity maximum ($\times 10^{-5}$ s^{-1})	12	20	26	27	27	35	37	61	62	60	59	57	62
	←──── shear vorticity on cyclonic side ──→ side of low-level jet					←──── vortex formation at 850 mb level ──→							

$(\zeta_\theta + f)\partial\theta/\partial p]$ are evident on the cyclonic side of the jet at this time, the maximum advection of PV is confined to a region over southern Nebraska and Kansas, where the flow along the jet axis is directed from higher to lower PV values (Fig. 8a). Bleck and Mattocks (1984) and Hoskins et al. (1985) show that the concept of "isentropic potential vorticity advection" (IPVA) is equivalent to the PVA (positive vorticity advection) rule in assessing the contributions of upper-level disturbances to surface development. The IPVA in Kansas and Nebraska ahead of the moving PV maximum over the northern plains (Fig. 8) indicates that the potential for vortex stretching and large-scale ascent at low levels exists ahead of the PV maximum. However, the existence of the extremely cold, stable air mass in the low levels acts to suppress surface development at this time. As will be shown, the surface development is delayed until the upper-level PV maximum is advected toward the coastal front/inverted trough along the East Coast.

The vertical cross section across the axis of the PJ at the initial time (Fig. 8c) shows that stratospheric values of PV [defined to be greater than 10×10^{-6} K mb^{-1} s^{-1} by Reed and Danielsen (1959)] extend downward within a region of strong subsidence centered on the warm side of an upper-tropospheric frontal zone. Numerous studies (Reed 1955; Reed and Danielsen 1959; Danielsen 1968; Shapiro 1970, 1975; Uccellini et al. 1985; Keyser and Shapiro 1986) have established that upper-level frontogenesis and tropopause folding are consequences of subsidence that is maximized beneath the axis of a jet streak and within and to the warm side of the developing frontal zone. The initial cross section through a relatively straight flow pattern (Fig. 8c) is consistent with the schematic presented by Danielsen (1968, his Fig. 14) for the vertical circulation pattern associated with tropopause folding and the diagnostic results derived from the two-dimensional

Sawyer-Eliassen circulation equation for this case by Uccellini et al. (1985).

The eastward propagation of the PJ-trough system toward the East Coast and the descent of the associated stratospheric extrusion between 12Z/18 and 03Z/19 are depicted in Figs. 9–11, which consist of 312 K isentropic analyses and vertical cross sections through the PJ as indicated in each figure. These isentropic maps and cross sections show: 1) the intensification of the simulated PJ between 12Z/18 and 00Z/19; 2) the intensifying middle- and upper-tropospheric frontal zone supporting the PJ upstream of and prior to the rapid cyclogenesis; 3) strong subsidence maximized within and along the warm side of the region of maximum baroclinicity; 4) descent of stratospheric values of PV within the frontal zone to near 700 mb by 03Z/19; and 5) the eastward propagation of the upper-level PV maximum and associated increase of the PV advection over the East Coast by 03Z/19 (Fig. 11b). The magnitude and location of the PJ, STJ, and PV extrusion at 00Z/19 simulated by model (Fig. 10) agree favorably with cross sections derived from radiosonde data at this time (Fig. 3). More importantly, the increased spatial and temporal resolution provided by the model data allows a distinct path to be traced following the eastward propagation and downward extrusion of the stratospheric air mass to a position several hundred kilometers northwest of the developing cyclonic circulation at 03Z/19. This path could only be inferred by Uccellini et al. (1985) using the operational radiosonde analyses and the once-per-day ozone measurements from the Total Ozone Mapping Spectrometer (TOMS). Finally, the propagation of the intensifying PJ through the short-wave trough is consistent with the "asymmetrical" thermal structure of upper-level troughs preceding cyclogenesis as described by Palmén and Newton (1969, pp. 335–338) and shown

in schematic form by Keyser and Shapiro (1986; see their Fig. 19).

c. Interaction of the stratospheric extrusion with a low-level PV maximum

The 300 K isentropic PV maps (Fig. 12) trace the descent of the stratospheric PV maximum between 06Z/19 and 15Z/19 and its interaction with a PV maximum confined to the lower troposphere along the coast. At 06Z/19, the stratospheric PV maximum is located over West Virginia at about 500 mb (Fig. 12a). By 09Z/19, a lower-tropospheric PV maximum becomes more evident along the Virginia coast (as the 300 K surface descends to higher pressure), with the stratospheric PV maximum approaching it from the west (Fig. 12b). The upper-level maximum appears to stall over northern Virginia and decrease slightly in magnitude, a characteristic that is likely due to diabatic effects associated with the expanding precipitation shield in this region (Fig. 6a). However, the southern portion of the upper-level PV maximum over central Virginia continues to move eastward down the sloping 300 K surface and the 10×10^{-6} K mb^{-1} s^{-1} isopleth and appears to merge with the low-level coastal PV maximum. By 12Z/19 (Fig. 12c), the two PV maxima on the 300 K surface are enclosed by a 14×10^{-6} K mb^{-1} s^{-1} isopleth. By 15Z/19 (Fig. 12d), a single PV maximum is evident off the Maryland coast.

The cross sections in Fig. 13 (denoted by the solid lines in Fig. 12) illustrate the superpositioning of the upper- and lower-tropospheric PV maxima above the developing surface cyclone during the rapid development phase. At 09Z/19 (Fig. 13b), the 10×10^{-6} K mb^{-1} s^{-1} isopleth of PV extends downward along the upper-tropospheric frontal zone toward the 700 mb level just to the northwest of the lower-level PV maximum. By 12Z/19, the 10×10^{-6} K mb^{-1} s^{-1} isopleths have connected. By 15Z/19, the upper-level PV maximum has almost overtaken the surface cyclone and the associated tongue of high PV extends directly over the low-level PV maximum (Fig. 13d).

d. Summary of the model simulation description

On the basis of Eulerian analyses presented in this section, it appears that the onset of rapid deepening of the surface cyclone in this simulation commences between 03Z/19 and 06Z/19 and proceeds through the rest of the model simulation to 00Z/20 (see Table 1). The rapid development in the model simulation is marked by 1) approximately 1.5 mb h^{-1} SLP decreases at the center of the storm after 06Z/19; 2) a transition in the vertical profile of the area-averaged mass divergence to a two-layer structure, with the maximum mass divergence amplifying within the 500–700 mb layer and the level of nondivergence becoming established at 700 mb; 3) an increase in the precipitation rates,
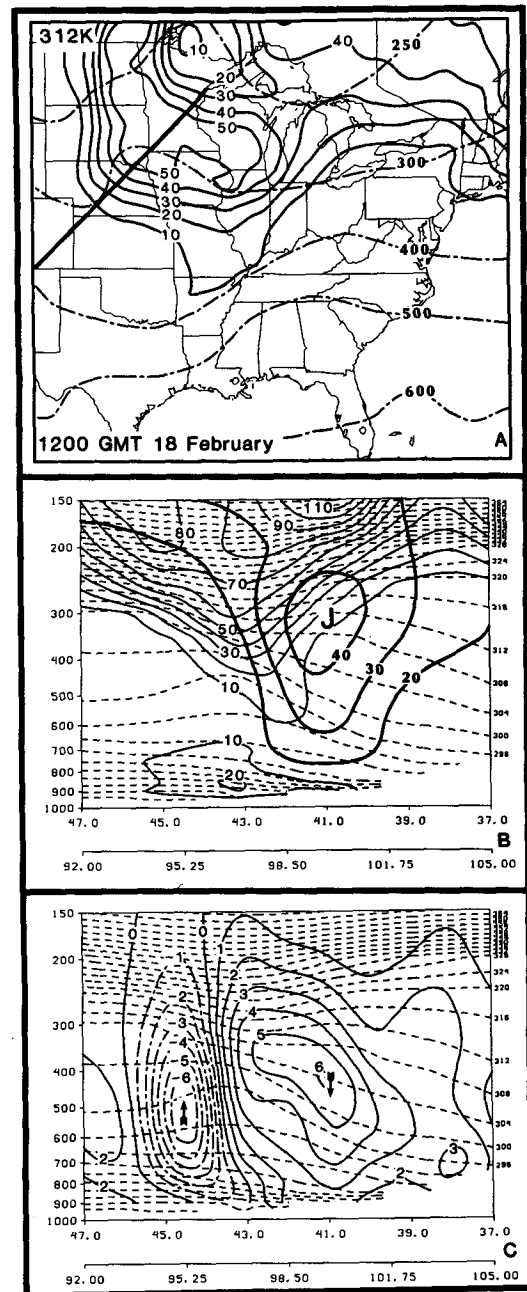

FIG. 8. Isentropic analyses for 312 K surface and vertical cross sections at the initial time (1200 UTC 18 February): (a) pressure (dot-dashed, mb) and potential vorticity (solid, $10 = 10 \times 10^{-6}$ K mb^{-1} s^{-1}), (b) isentropes (dashed, K), potential vorticity (thin solid, $10 = 10 \times 10^{-6}$ K mb^{-1} s^{-1}) and isotachs (heavy solid, m s^{-1}), and (c) isentropes (dashed, K) and omega [(solid-positive, dashed-negative (μb s^{-1})]. The "J" in (b) indicates position of jet core. Line in (a) indicates the position of cross section. Arrows in (c) denote direction of vertical motion.

especially those associated with the grid-resolvable precipitation between 06Z and 09Z just to the north and west of the storm center (see Fig. 5 and Table 1);
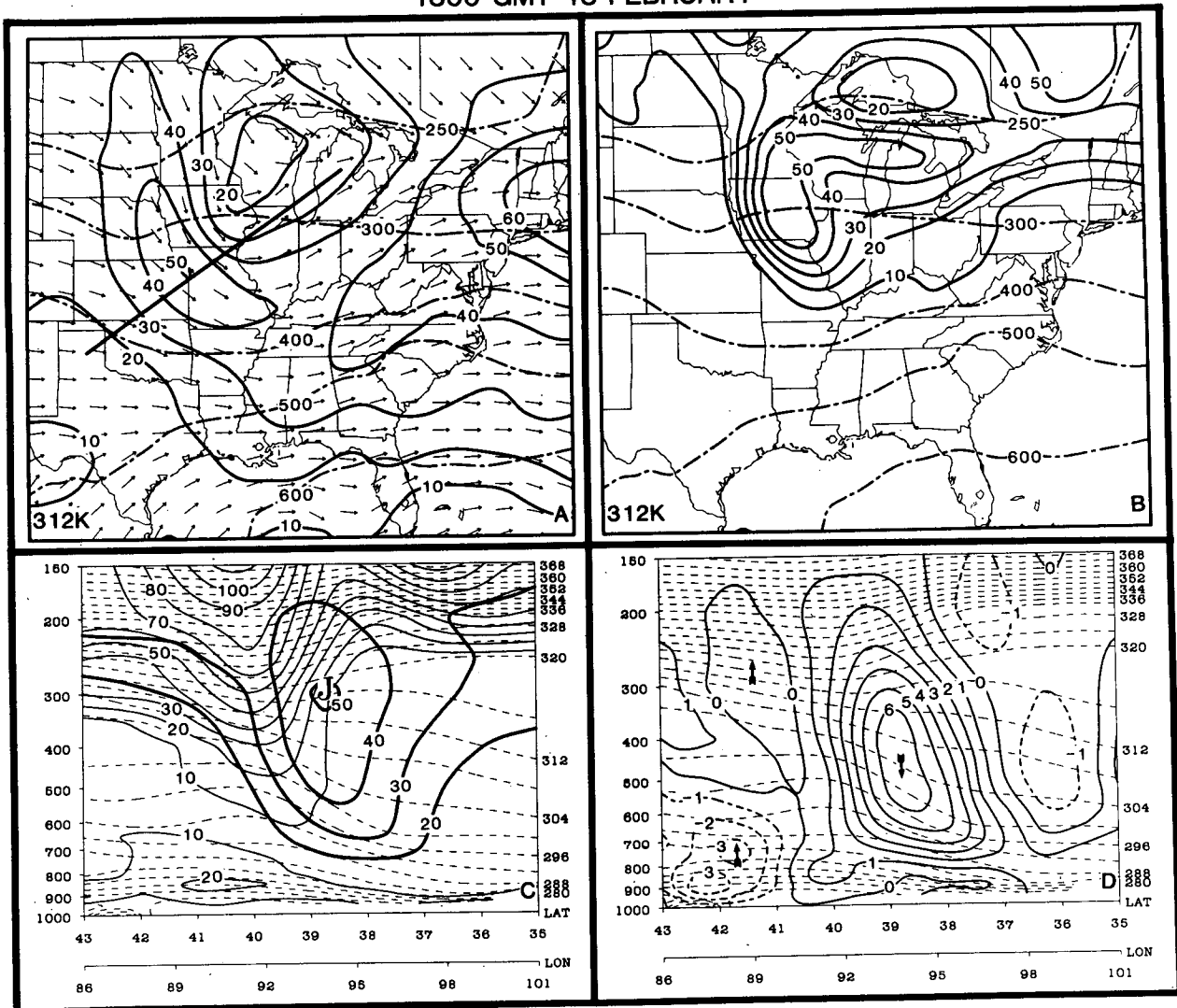
1800 GMT 18 FEBRUARY

FIG. 9. Isentropic analyses for 312 K surface and vertical cross sections at 6 h (1800 UTC 18 February): (a) isotachs (solid, m s⁻¹), pressure (dot-dashed, mb), and arrows to indicate wind direction; (b) pressure (dot-dashed, mb) and potential vorticity (solid, $10 = 10 \times 10^{-6}$ K mb⁻¹ s⁻¹; (c) isentropes (dashed, K), potential vorticity (thin solid, $10 = 10 \times 10^{-6}$ K mb⁻¹ s⁻¹) and isotachs (heavy solid, m s⁻¹); and (d) isentropes (dashed, K) and omega [solid-positive, dashed-negative (μb s⁻¹)]. The "J" in (c) indicates position of jet core. Line in (a) indicates position of cross section. Arrows in (d) denote direction of vertical motion.

and 4) an increase in the PV advection aloft (associated with the stratospheric extrusion) over a low-level PV maximum (associated with the coastal front and inverted trough). The interaction of separate, upper- and lower-tropospheric PV maxima during the period of rapid surface development is consistent with the observations discussed for this case by Bosart and Lin (1984) and Uccellini et al. (1985) and also with recent diagnostic analyses of other cyclone events by Gyakum (1983) and Boyle and Bosart (1986).

Table 1 also shows that the rapid deepening of the simulated storm system is marked by an increase in the 850 mb absolute vorticity from 37×10^{-5} s⁻¹ at

06Z/19 to 56 and 62×10^{-5} s⁻¹ at 09Z/19 and 12Z/19, respectively. Eulerian and Lagrangian diagnostics are presented in the following sections to 1) investigate the processes that contribute to the rapid increase of lower-tropospheric absolute vorticity between 06Z/19 and 09Z/19, and 2) illustrate the nature and origin of different airstreams which converge into the rapidly developing low-level circulation during the rapid development phase.

5. Vorticity diagnostics from a Eulerian perspective

The vertical component of the inviscid vorticity equation in pressure coordinates is
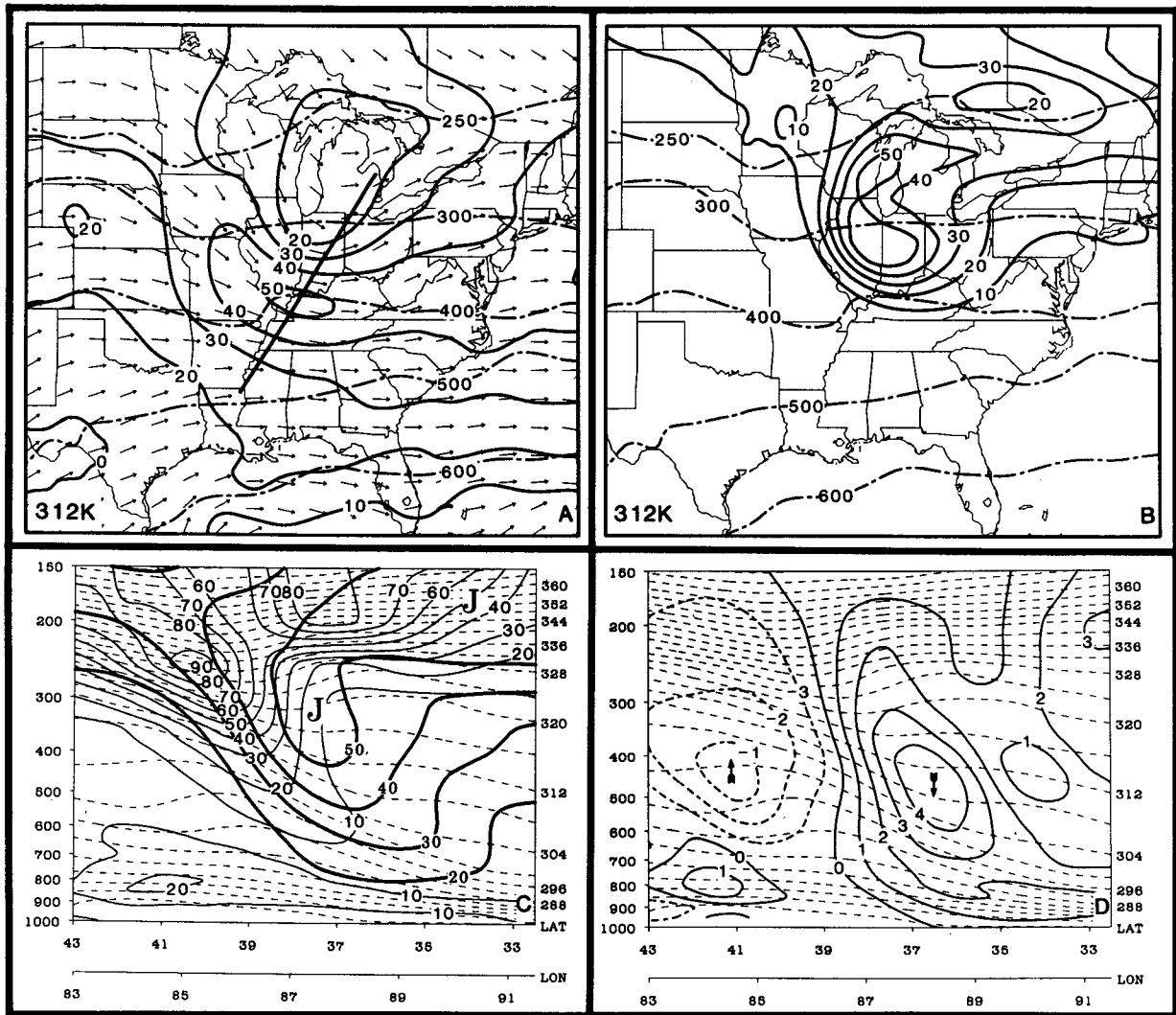
0000 GMT 19 FEBRUARY

FIG. 10. As in Fig. 9, but at 12 h (0000 UTC 19 February).

$$\frac{\partial(\zeta p + f)}{\partial t} = -\mathbf{V} \cdot \nabla(\zeta p + f) - \omega \frac{\partial \zeta p}{\partial p}$$

$$- (\zeta p + f)\nabla \cdot \mathbf{V} - \mathbf{k} \cdot \left(\nabla \omega \times \frac{\partial \mathbf{V}}{\partial p} \right), \quad (2)$$

where ζp is the vertical component of the relative vorticity, $(\zeta p + f)$ the absolute vorticity and $\mathbf{V}$ the horizontal wind vector. The four terms on the right-hand side of Eq. (2) will hereafter be referred to as the horizontal advection, vertical advection, stretching, and tilting terms.

The 850 mb absolute vorticity undergoes a rapid change between 06Z/19 and 12Z/19 (Fig. 14). The magnitude of the 850 mb vorticity maximum nearly doubles between 06Z/19 and 09Z/19 and increases to

62×10^{-5} s^{-1} by 12Z/19 (Table 1). To assess the relative magnitude of the separate terms in Eq. (2) and their contribution to the 850 mb vorticity increase, a vertical cross section for 12Z/19 is depicted in Fig. 15 (the line for the cross section on the map inset is shown in Figs. 15a and 15b). The maximum vorticity is located below 700 mb at 12Z/19 and decreases rapidly between the 700 and 600 mb levels. The rapid decrease of vorticity with height is due, in part, to the north–south orientation of the cross section through a vorticity maximum which is tilted toward the northwest with height. The vorticity tendency is maximized below 700 mb (Fig. 15b), due to the dominance of stretching at lower levels (Fig. 15e), a result which is consistent with other diagnostic studies of cyclogenesis [e.g., Newton (1956)]. Above 700 mb, the stretching term becomes negative,
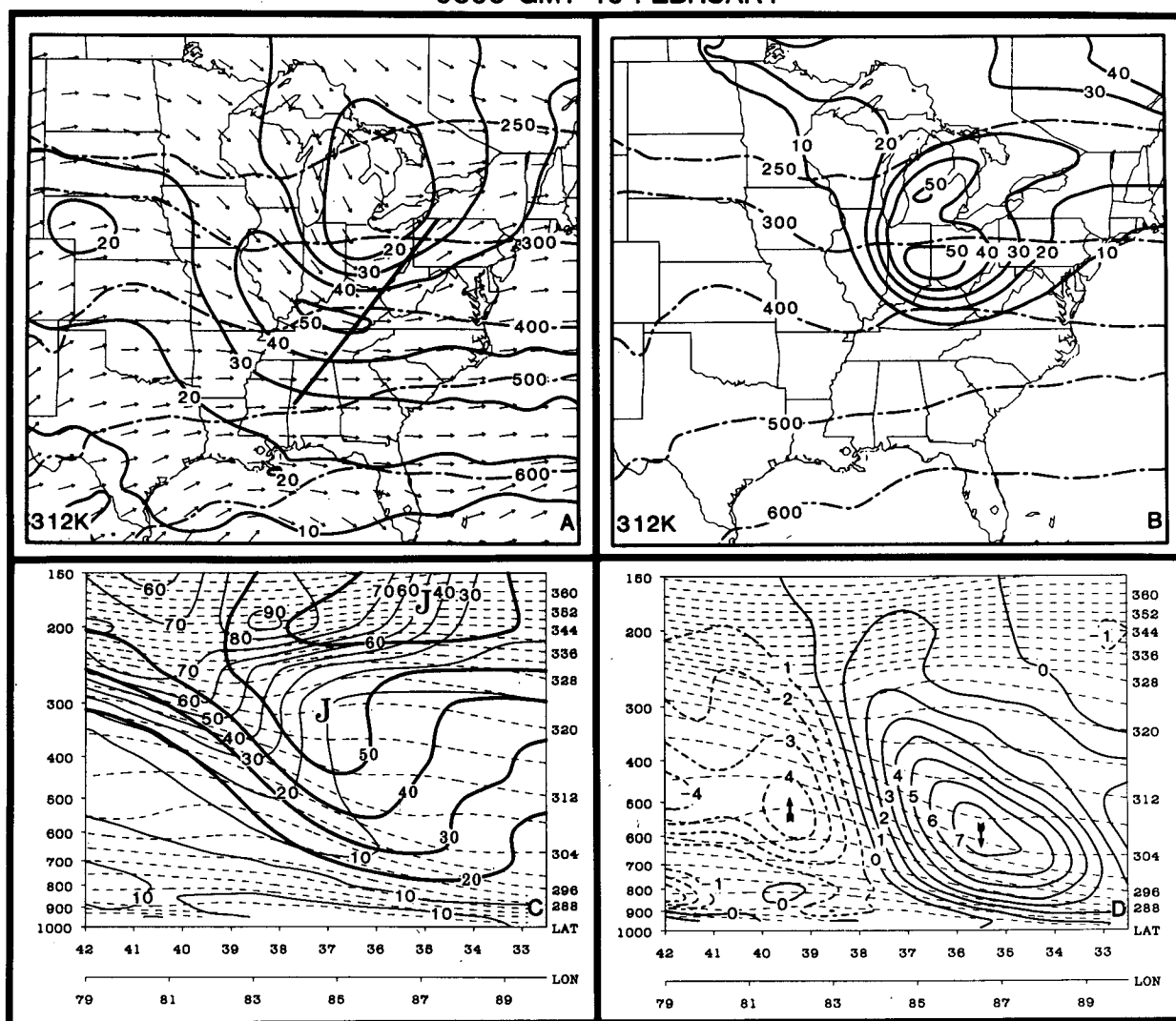
0300 GMT 19 FEBRUARY

FIG. 11. As in Fig. 9 but at 15 h (0300 UTC 19 February).

which is consistent with the increasing mass divergence in the middle to upper troposphere (Fig. 7g). The horizontal vorticity advection is positive in the middle troposphere ahead of the advancing short-wave trough, indicating that the favorable quasi-geostrophic forcing diagnosed by Bosart and Lin (1984) also exists above the simulated surface low at this time. The tilting term is also positive to the south and east of the developing storm. Finally, the vertical advection term is large in the 700 to 500 mb layer in association with the strong ascent maximum just northeast of the surface low (Fig. 6) in a region of significant precipitation. It appears that the ascent maximum is responsible for advecting large values of vorticity (concentrated in the lower troposphere by stretching) upward into the middle troposphere (although this effect is offset by negative

stretching in the middle troposphere). This result is consistent with the Johnson and Downey (1976) angular momentum budget study which shows that, for an extratropical cyclone, the midlevel vortex develops and is maintained, in part, due to the vertical transport of absolute angular momentum by a meridional mass circulation enhanced by the release of latent heat.

6. Diagnostics from a Lagrangian perspective and the analysis of various airstreams during rapid cyclogenesis

From the analyses in section 4 and the summary in Table 1, it appears that the rapid decrease in the SLP and the increase in the lower-tropospheric vorticity occur as an upper-tropospheric PV maximum associated with a tropopause fold was advected toward a lower-
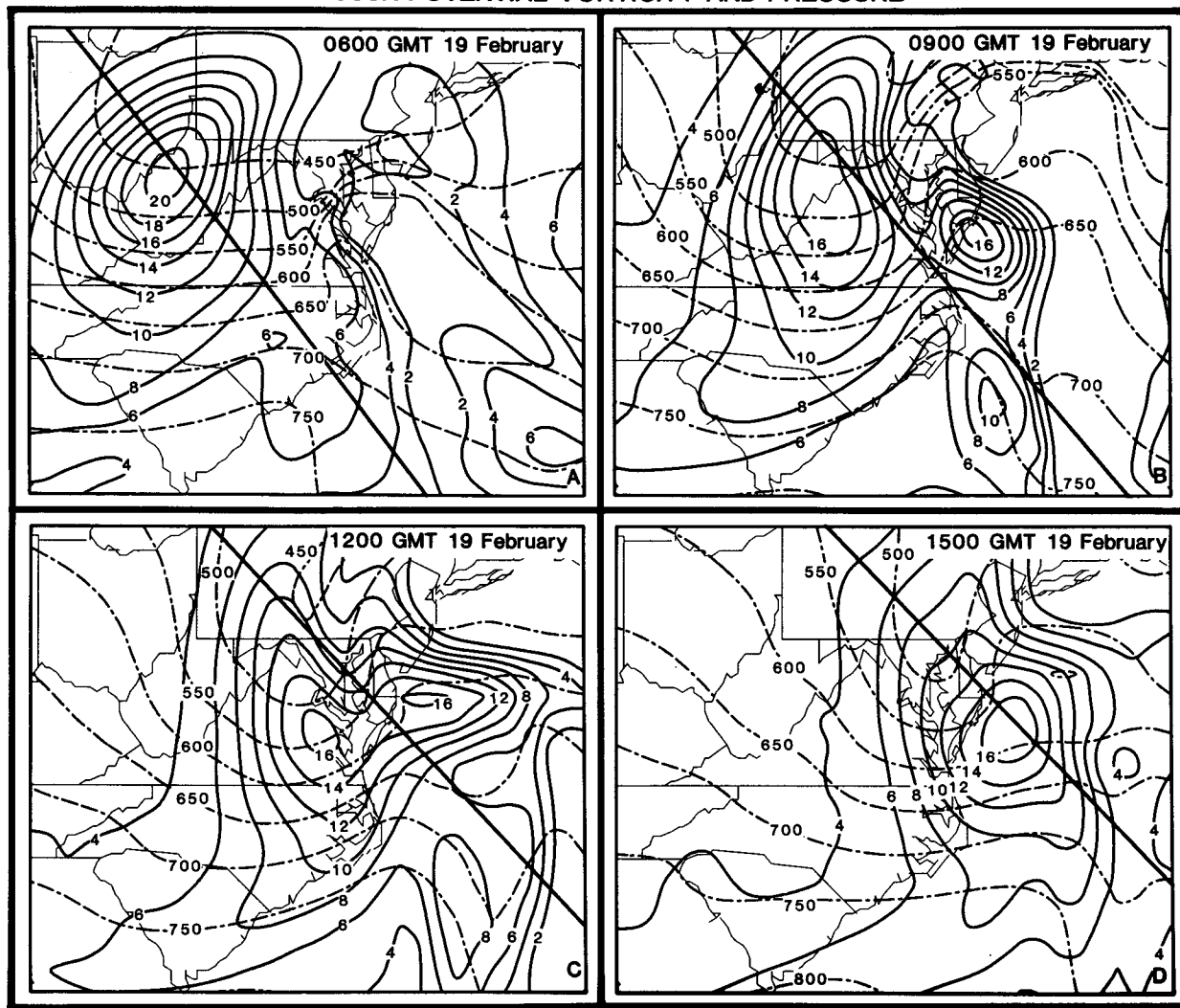
300K POTENTIAL VORTICITY AND PRESSURE

FIG. 12. The 300 K analyses of potential vorticity (solid, $10 = 10 \times 10^{-6}$ K mb^{-1} s^{-1}) and pressure (dot-dashed, mb) at (a) 18 h (0600 UTC 19 February), (b) 21 h (0900 UTC 19 February), (c) 24 h (1200 UTC 19 February), and (d) 27 h (1500 UTC 19 February). Lines indicate position of cross sections in Fig. 13.

tropospheric PV maximum associated with the coastal front. Trajectories are now presented to depict this interaction before and during the rapid development phase of the Presidents' Day storm and to provide insight into the origin of airstreams which converge into the cyclogenetic region. Furthermore, model-dependent variables and various diagnosed quantities are interpolated from the grid to parcel positions to study the dynamic and thermodynamic processes which influence the parcels as they approach the developing storm system. Included in the analysis are the vorticity changes following a parcel,

$$\frac{d(\zeta_p + f)}{dt} = -(\zeta_p + f)\nabla_p \cdot \mathbf{V} - \mathbf{k} \cdot \left(\nabla \omega \times \frac{\partial \mathbf{V}}{\partial p} \right), \quad (3)$$

to determine the relative contributions of stretching [term (1)] and tilting [term (2)] along the various airstreams as they converge toward the developing cyclone.

a. Trajectories computed backward in time from the region of surface cyclogenesis

A history file containing data at 15 min intervals during the model integration is used to compute *backward trajectories* for 40 parcels initialized on a 2° by 2° box surrounding the developing surface low and the 850 mb vorticity tendency maximum at 03Z/19, 06Z/ 19, 09Z/19, and 12Z/19 (Fig. 16). Trajectories were computed backward to the initial time (12Z/18) using
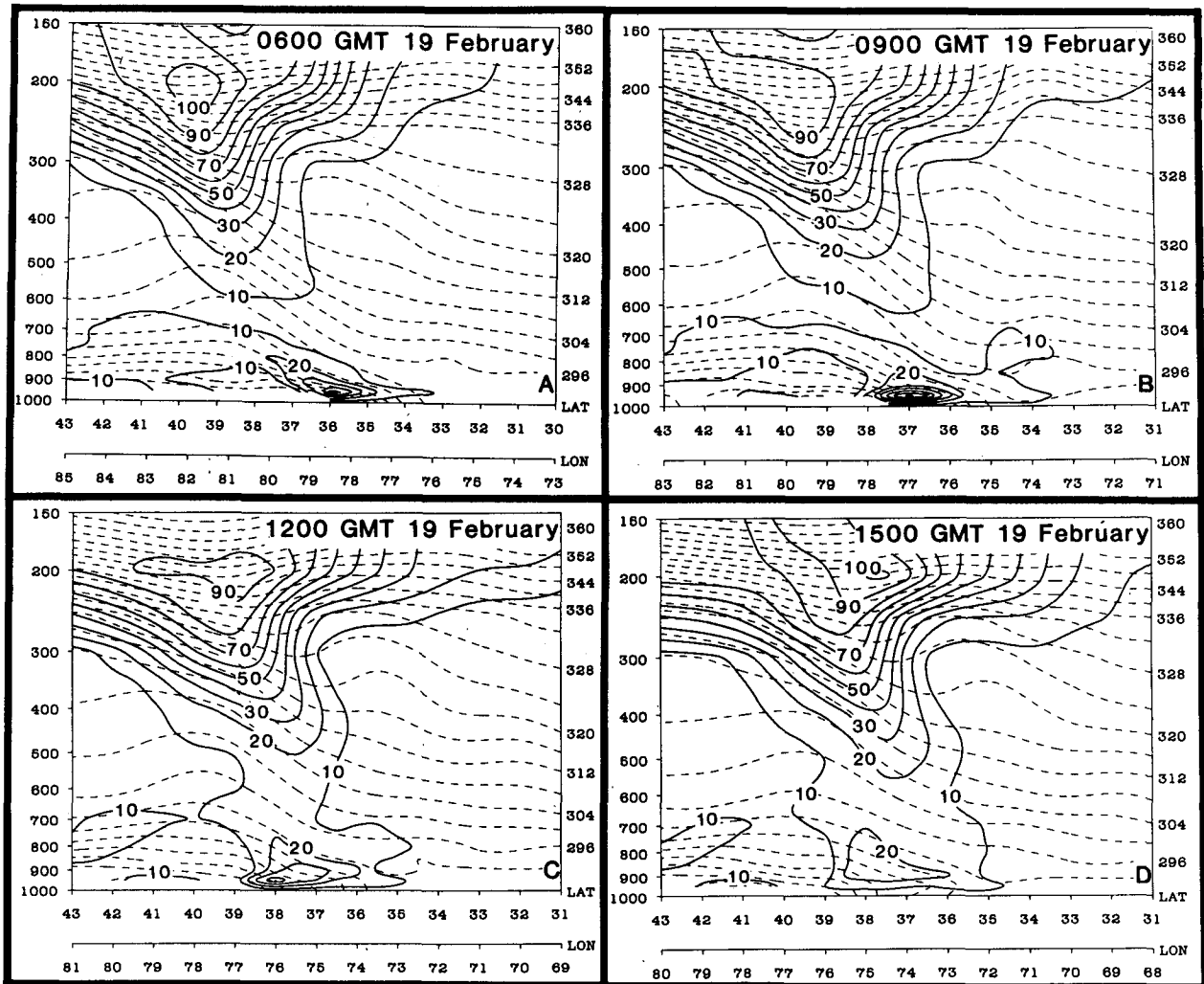
FIG. 13. Vertical cross sections of potential temperature (dashed, K) and potential vorticity (solid, $10 = 10 \times 10^{-6}$ K mb^{-1} s^{-1}) at (a) 18 h (0600 UTC 19 February), (b) 21 h (0900 UTC 19 February), (c) 24 h (1200 UTC 19 February), and (d) 27 h (1500 UTC 19 February). Lines in Fig. 12 indicate positions of cross sections.

the archived u, v, and omega data.[3] The backward trajectories from the box located at 700 mb initialized at 03Z/19 and 06Z/19 (Figs. 16a and b) show that during this period the air within the entire storm volume at the 700 mb level originates from within the oceanic PBL at levels ranging from 880 to 985 mb. These parcels ascend and accelerate toward the developing storm system beneath the region of, and probably in response to, the mass flux divergence that is contributing to the decreasing SLP within the box (see Figs. 7c, d, and e).

---

[3] New parcel positions were computed using an iterative method. A first-guess position is obtained by advecting the parcel (forward or backward) with the velocity components at the original position. New velocity components (obtained by interpolating to the first-guess position) are averaged with the old velocity components, and an updated position is obtained by advecting the parcel again with the updated velocities. This process was repeated three times for each time step.

Between 06Z/19 and 09Z/19 (Fig. 16c), a major transition has occurred with the arrival of the airstream from the west-southwest into the region of what is now a rapidly developing cyclone, a transition that is also marked by the sudden doubling of the 850 mb vorticity during the same period (Table 1). This airstream originates from near the 500 mb level within the PJ/tropopause fold region in the central United States and approaches the storm from the southwest while the ocean-influenced airstreams dominate the southeastern, eastern, and northern sides of the storm system. During the 3-h period ending at 12Z/19, the airstream originating near the 400 mb level within the PV maximum (associated with the tropopause fold) and descending toward the storm center becomes an increasingly important component of the storm system (Fig. 16d).

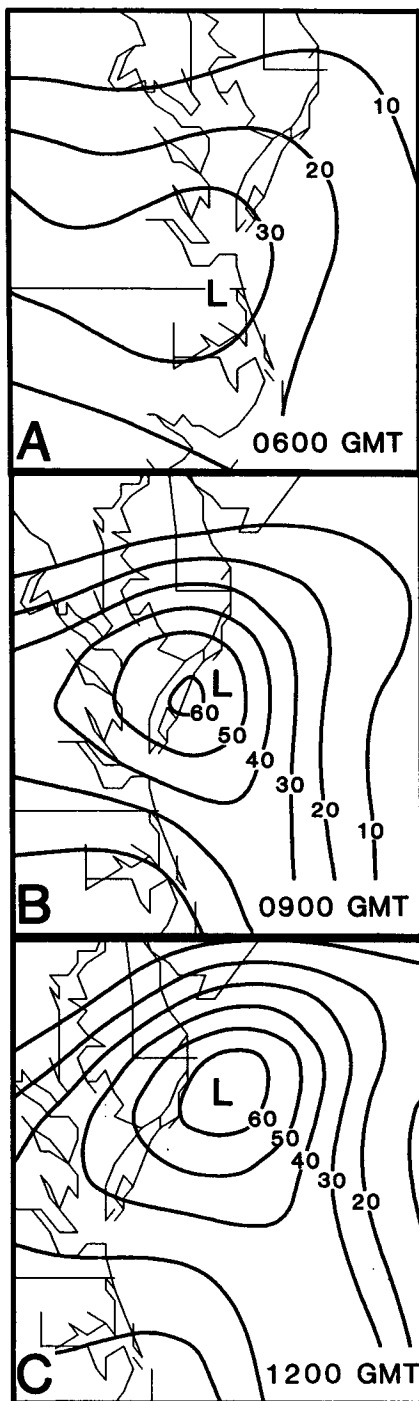The model-based trajectories confirm that the rapid

FIG. 14. The 850 mb vorticity analyses ($10 = 10 \times 10^{-5}$ s^{-1}) at (a) 18 h (0600 UTC 19 February), (b) 21 h (0900 UTC 19 February) and (c) 24 h (1200 UTC 19 February). The L indicates the position of the surface low center.

development phase of the Presidents' Day cyclone commenced as several airstreams converged toward the storm center. Carlson (1980) describes these airstreams

as the "dry airstream" descending from the west-southwest [see also Danielsen (1974) and Carr and Millard (1985)], a "cold conveyor belt" ascending from the east, and a "warm conveyor belt" ascending from the south of the storm [see also Browning (1971) and Browning and Harrold (1969)]. Although the warm conveyor belt appears to be comparatively weak (made up of only 3 out of the 40 parcels in Fig. 16d), its ascent to the 700 mb level to a position on the northern boundary of the box at 12Z/19 is in agreement with the trajectories computed from the radiosonde data base and described by Uccellini et al. (1985).

Backward trajectories (Fig. 17) for parcels located at the 800 mb (Fig. 17a), 850 mb (Fig. 17b), and 900 mb (Fig. 17c) levels surrounding the storm system at 12Z/19 show the vertical extent of the stratospheric extrusion and its interaction with the other airstreams at this time. The dry airstream descending into the southwestern quadrant is still evident at the 800 mb level (Fig. 17a). Fewer trajectories initialized at the 850 mb level near the storm center at 12Z/19 are associated with the dry airstream, and these do not trace back to as low a pressure level as those initialized at 800 mb. At the 900 mb level, most of the representative air parcels moving through the storm system at 12Z/19 originate within the oceanic PBL (Fig. 17c) in the strong surface anticyclone north and east of the developing storm 24 h earlier. These parcels descend anticyclonically as they move southward, then turn westward, accelerate, and begin ascending as they approach the storm, representing the cold conveyor belt as described earlier. The trajectories which originate at low levels to the south of the storm move into the carolinas and suddenly become directed eastward toward the storm center as the stratospheric air arrives over this area at higher levels (as shown in Figs. 16c and 16d).

Representative trajectories selected from the dry airstream, cold conveyor belt, and warm conveyor belt are shown in Figs. 18a and b. In the remainder of the section, these trajectories, along with diagnostic quantities presented in tabular form, are described in more detail to provide insight into how these different airstreams interact and contribute to the development of the simulated storm system.

b. Trajectory diagnostics for the dry airstream

A subset of the trajectories representative of the dry airstream is illustrated in Fig. 18a.[4] Trajectories 1 through 3 were initialized on the 296 K surface below the axis of the PJ over the northern plains at 12Z/18 and were computed forward in time for 36 h. These trajectories spread out as they descend and move east-

---

[4] Another subset of the dry airstream trajectories that move at a slower rate than those shown in Fig. 19a and go through several cycles of interaction with the PJ-trough system is described in the Appendix.

1200 GMT 19 FEBRUARY
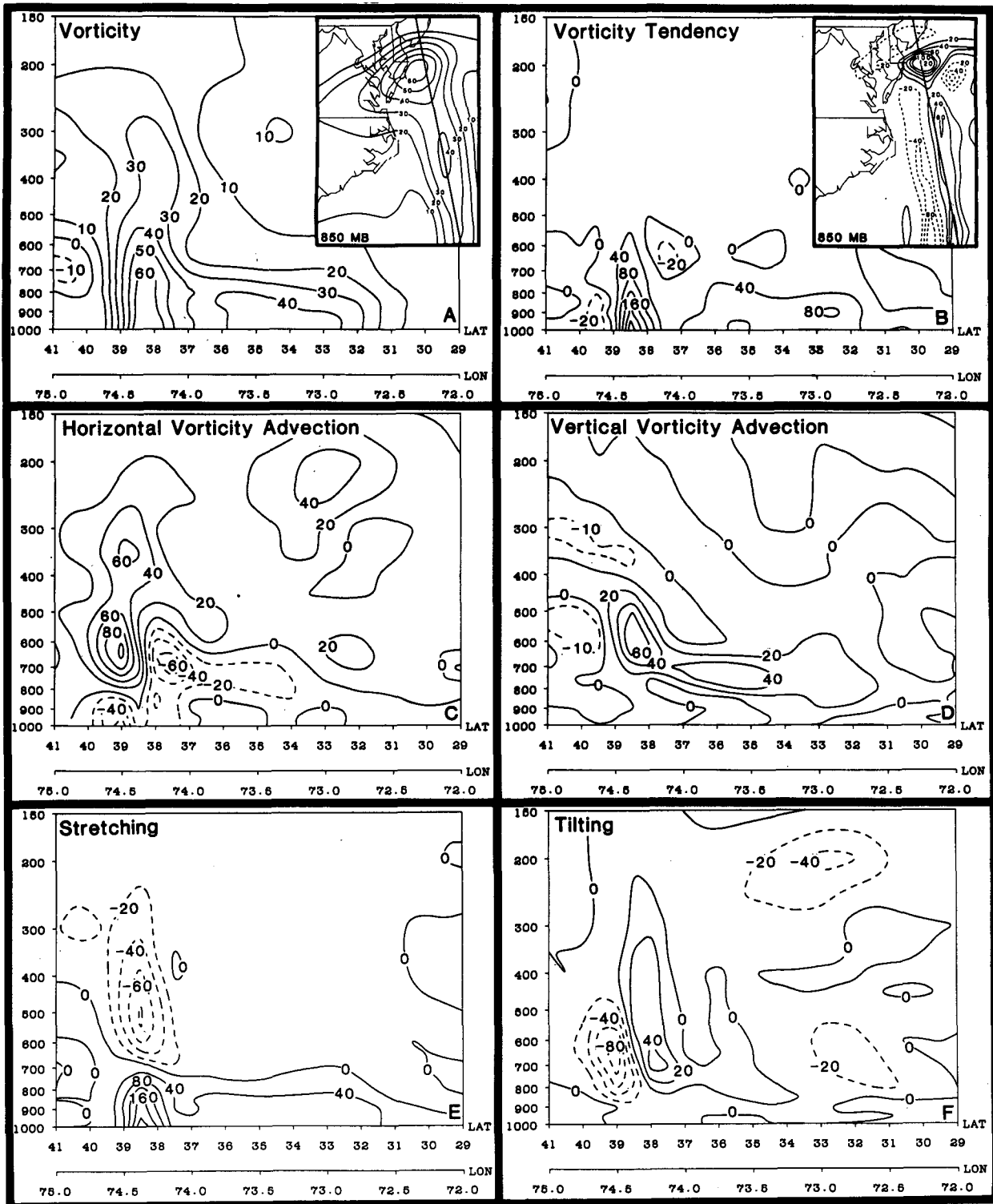
FIG. 15. Cross sections at 24 h (1200 UTC 19 February) of (a) absolute vorticity, (b) vorticity tendency, (c) horizontal advection of vorticity, (d) vertical advection of vorticity, (e) stretching, and (f) tilting. In (a), $10 = 10 \times 10^{-5}$ s^{-1}; in (b), (c), (d), (e), and (f), $10 = 10 \times 10^{-9}$ s^{-2}. The position of the cross section is denoted by the solid line in the 850 mb vorticity and vorticity tendency analyses in the map insets in (a) and (b), respectively.
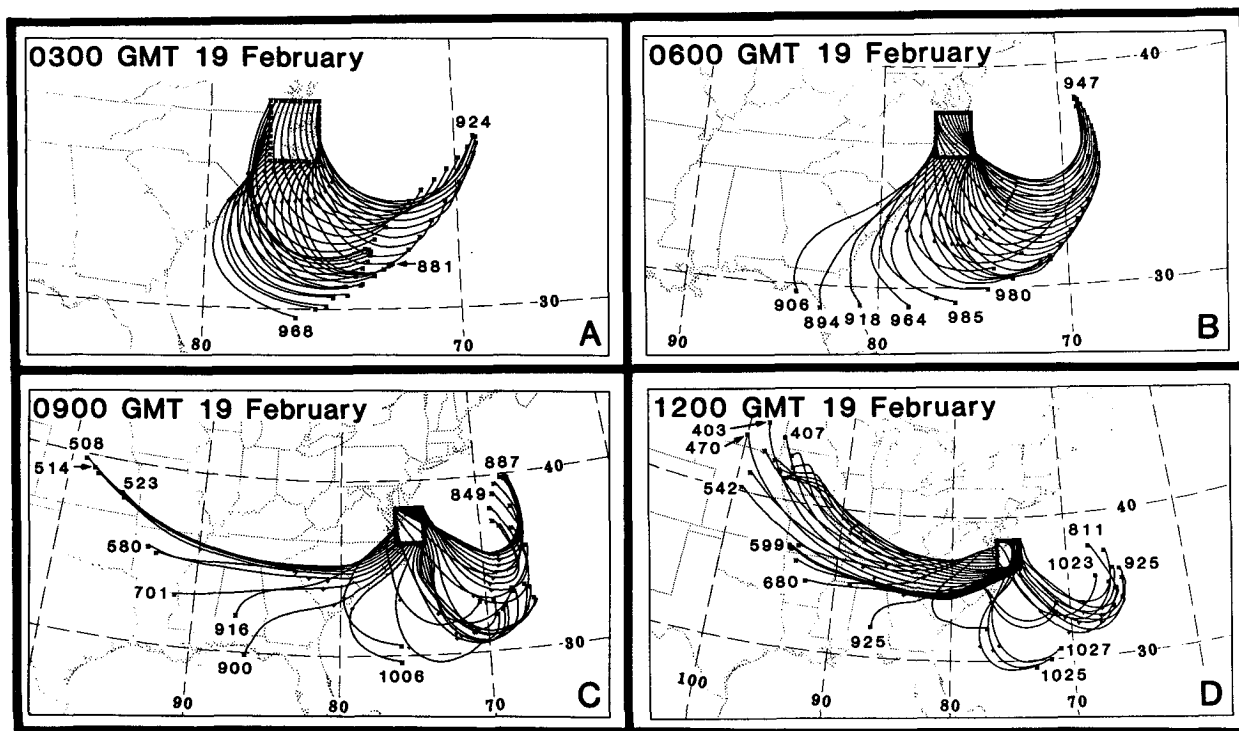
FIG. 16. Paths of 40 model trajectories initialized on a 2° by 2° box surrounding the maximum of vorticity tendency on the 700 mb level at (a) 0300 UTC 19 February, (b) 0600 UTC 19 February, (c) 0900 UTC 19 February, and (d) 1200 UTC 19 February computed backward in time to 1200 UTC 18 February. The pressure in millibars is given at the beginning point of selected trajectories.

southeastward, consistent with the schematic for typical trajectories which accompany tropopause folding presented by Danielsen (1980, his Fig. 12) and with the trajectories computed for this case using the operational radiosonde data base (Uccellini et al. 1985; their Fig. 17). Trajectory 1 moves through the trough system as it descends to near the 500 mb level over West Virginia (at 18 h), turns anticyclonically and ascends through the upper-level ridge over New England, and enters the polar jet over southeastern Canada. Trajectory 2 experiences strong subsidence on the west side of the trough, descends along a cyclonically curved path over the central United States on 18 February, and, by 12Z/19, approaches the rapidly developing storm system from the southwest. The parcel descends to 761 mb before it rises rapidly east of the storm system while turning anticyclonically and joining the westerly flow near the upper-level ridge northeast of the surface low. Trajectory 3 decelerates on the western side of the trough system as the parcel exits the PJ on 18 February and descends to the 860 mb level off the Florida coast by 00Z/20.

Trajectory 2 was chosen to represent parcels which trace back from the southwestern quadrant of the developing storm at 15Z/19 to the tropopause fold over the northern plains 27 h earlier. Diagnostic variables interpolated to the parcel positions are listed in Table

2. This trajectory originates at 470 mb over western Iowa, below the axis of the intensifying PJ and within the stratospheric extrusion associated with the tropopause fold as indicated by the high PV value (13.1 $\times$ 10^{-6} K mb^{-1} s^{-1}) and low specific humidity [0.2 g kg^{-1} (not shown)]. Between 16Z/18 and 06Z/19, the parcel is sinking at rates ranging from 4.0 to 7.3 μb s^{-1}, indicating that it is well within the region of maximum subsidence on the warm side of the upper-level front that brings the parcel down to 672 mb by 06Z/19.

The PV and potential temperature changes for trajectory 2 are small as the parcel descends to the 761 mb level by 12Z/19. Since computed PV gradients are so strong in the frontal zone, even small errors related to the interpolation procedure or inaccuracies in the trajectory computation could be contributing to changes in the value of PV and θ interpolated to the parcel position.

As the parcel descends, the isobaric absolute vorticity increases slightly due to weak positive stretching and tilting, reaching a value of 25.4 $\times$ 10^{-5} s^{-1} at 00Z/19. From 00Z/19 to 12Z/19, the parcel remains in a region of divergence, and the absolute vorticity decreases to 18.3 $\times$ 10^{-5} s^{-1} by 12Z/19 due to negative stretching. Between 12Z/19 and 15Z/19, the PV, θ, $\zeta + f$, and the stretching term all increase. The PV increases to a value

1200 GMT 19 FEBRUARY
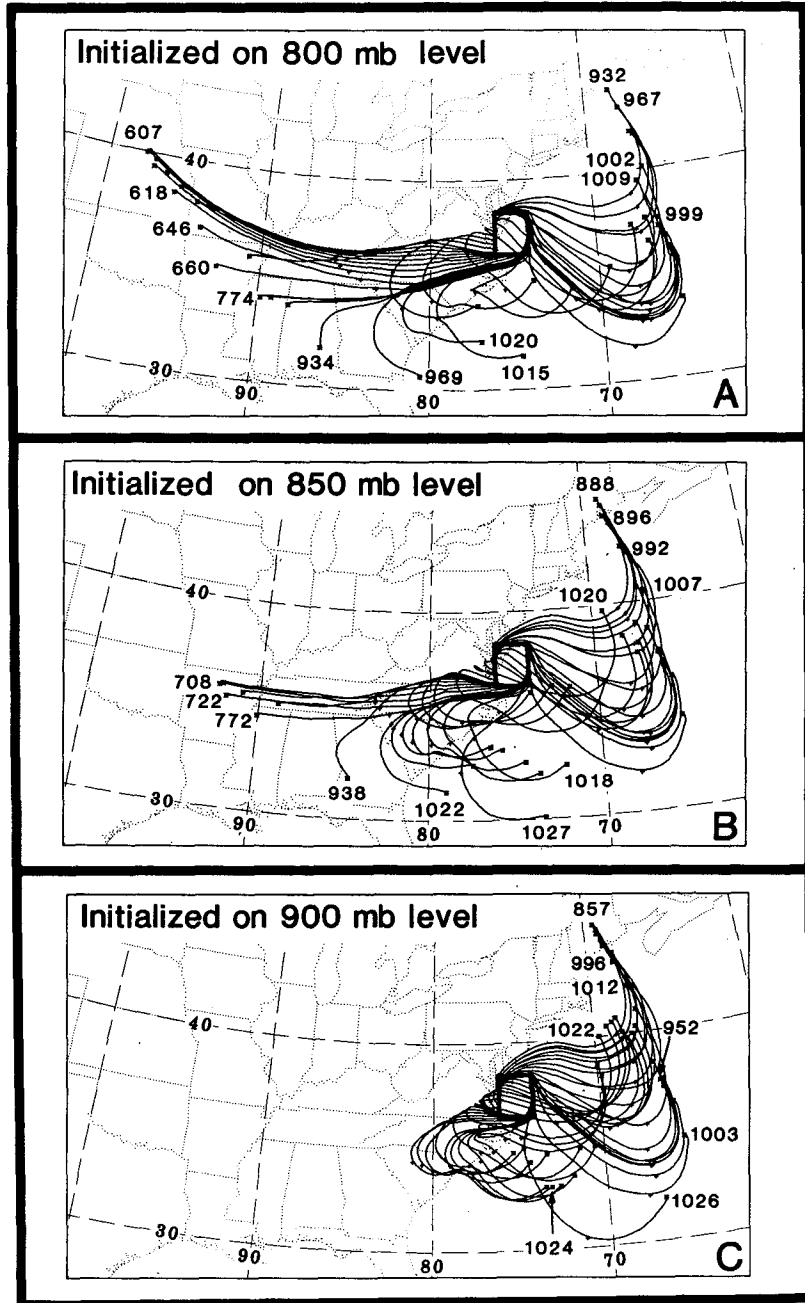
FIG. 17. Paths of trajectories initialized at (a) 800 mb, (b) 850 mb, and (c) 900 mb at 1200 UTC 19 February and computed backward in time for 24 h. Pressure in millibars is given at the beginning point of selected trajectories.

of 15.1×10^{-6} K mb^{-1} s^{-1} by 15Z/19, while the static stability decreases from 0.065 K mb^{-1} at 12Z/19 to 0.053 K mb^{-1} at 15Z/19, indicating that the parcel is entering the boundary layer PV maximum along the East Coast (Fig. 13c). At the same time, the stretching term increases from 0.7×10^{-9} s^{-2} to as high as 13.2
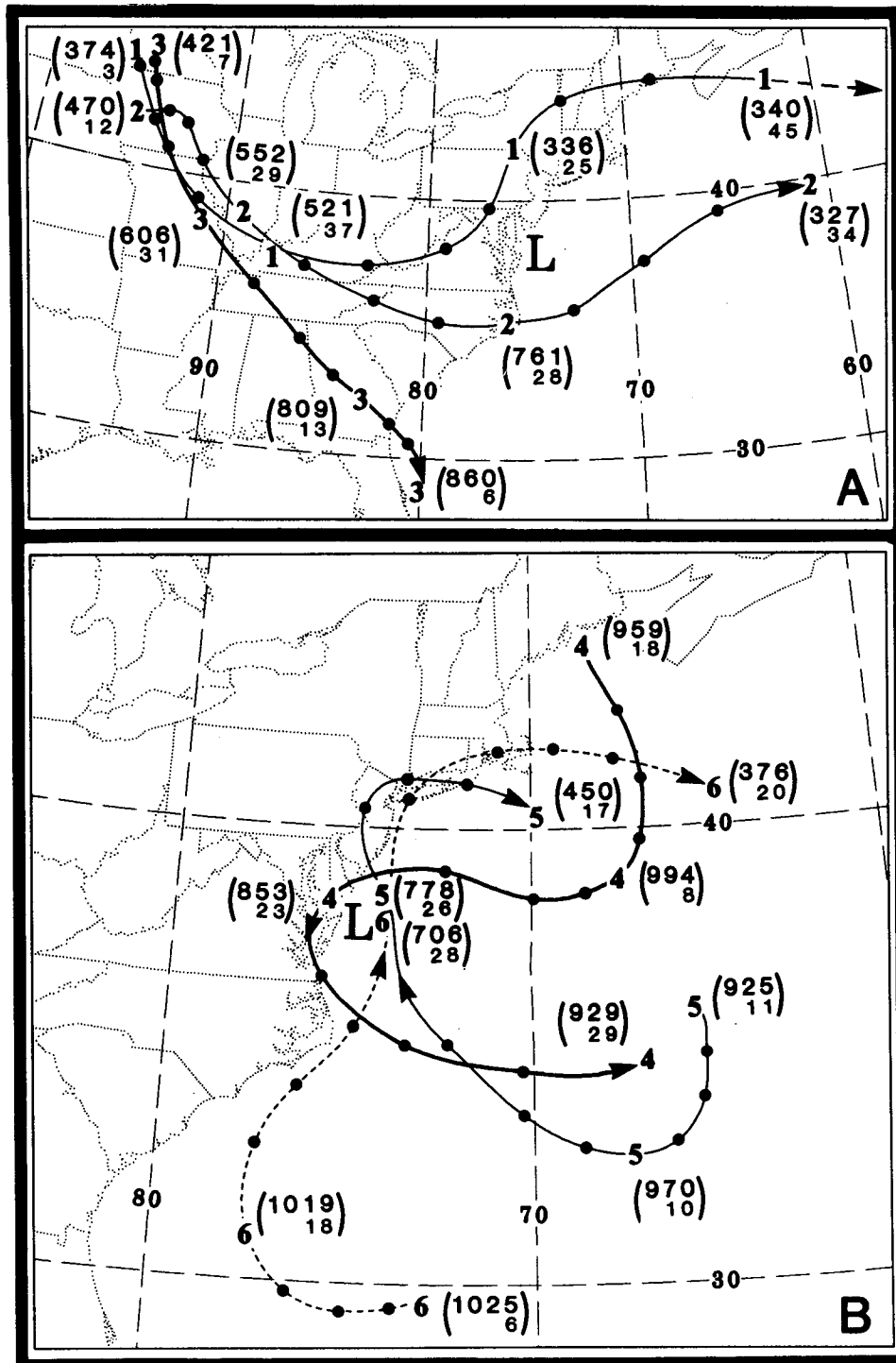
FIG. 18. A collection of six 36-h trajectories computed forward from 1200 UTC 18 February. Trajectory numbers (1–6, bold) are placed at 12-h intervals along the trajectory. Large dots mark 3-h positions. Pressure (millibars) and speed (meters per second) are given inside parentheses at 12-h intervals. The "L" denotes position of surface low at 1200 UTC 19 February.

TABLE 2. Listing for the dry airstream trajectory (trajectory 2 in Fig. 18a) for the times and dates listed in the left-hand column. The variables include pressure (p, mb), potential temperature (θ, K), wind speed (m s^{-1}), isentropic absolute vorticity ($\zeta_\theta + f$, 10^{-5} s^{-1}), static stability ($-\partial\theta/\partial p$, K mb^{-1}), potential vorticity (PV, $10 = 10 \times 10^{-6}$ K mb^{-1} s^{-1}), isobaric absolute vorticity ($\zeta_p + f$, 10^{-5} s^{-1}), and the stretching and tilting terms interpolated to parcel positions ($10 = 10 \times 10^{-9}$ s^{-2}).

| Time/ date	Lat	Long	p	θ	Speed	$\zeta_\theta + f$	$-\partial\theta/\partial p$	PV	$\zeta_p + f$	Stretch	Tilt
12Z/18	42.0	95.0	470	296.0	12	22.3	0.059	13.1	23.1	4.5	1.2
00Z/19	38.8	89.3	552	296.9	28	20.3	0.069	14.0	25.4	−4.7	1.5
06Z/19	36.0	82.5	672	297.3	28	12.5	0.088	11.1	17.4	−1.6	0.6
12Z/19	35.2	76.1	761	297.1	28	16.0	0.065	10.4	18.3	0.7	−3.4
14Z/19	35.5	73.8	754	297.0	26	19.0	0.061	11.6	20.9	13.2	−9.8
1430Z/19	35.6	73.3	741	297.4	25	25.4	0.056	14.2	27.6	11.3	−2.0
15Z/19	35.8	72.8	714	298.5	26	28.3	0.053	15.1	31.5	−2.0	14.8
1530Z/19	36.1	72.3	671	300.4	30	25.0	0.051	12.8	29.7	−20.9	21.2
16Z/19	36.4	71.7	616	302.6	34	18.3	0.055	10.1	22.7	−25.2	1.3
1630Z/19	36.8	71.1	564	304.8	36	14.1	0.056	7.8	17.2	−10.9	−14.9
18Z/19	37.6	69.3	459	307.0	29	14.1	0.049	6.9	19.5	4.0	0.8

$\times 10^{-9}$ s^{-2} at 14Z/19, as the parcel begins to accelerate up and out of the storm system. The tilting term does not contribute appreciably to the spinup associated with this airstream. At 1500Z/19, the parcel attains a maximum absolute vorticity of 31.2×10^{-5} s^{-1} at a pressure of 714 mb. The vorticity then decreases as the parcel rises through a layer of strong divergence above 700 mb (as indicated by the negative stretching after 15Z/19 in Table 2), decreasing to 19×10^{-5} s^{-1} by 18Z/19 as the parcel ascends to 459 mb northeast of the surface cyclone.

c. Trajectory diagnostics for the cold conveyor belt

Trajectories 4 and 5 (Fig. 18b) are part of the cold conveyor belt that originates in the lower troposphere within the strong anticyclone poised to the north and east of the developing storm system. Parcel 4 (tabulated diagnostics not shown) descends to the 994 mb level by 00Z/19, then turns toward the west, accelerates from 13 to 30 m s^{-1} between 06Z/19 and 10Z/19, and rises to the 850 mb level as it passes north of the storm center. This parcel enters the developing low-level cyclonic circulation after 09Z/19, attaining an absolute vorticity value of 4.4×10^{-4} s^{-1} by 12Z/19. The parcel loops around the storm center between 12Z/19 and 18Z/19 and is directed toward the east over the ocean during the last 6 h of the model simulation.

Parcel 5 in Fig. 18b also originates within the cold anticyclonic circulation to the east of the developing storm system. As the parcel approaches the cyclone between 12Z/18 and 06Z/19, the potential temperature and mixing ratio increase by 9.4 K and 4.5 g kg^{-1}, respectively, due to the heat and moisture fluxes in the ocean-influenced PBL (Table 3). The parcel also begins to accelerate, with the wind speed increasing from 12.0 to 17.6 m s^{-1} between 03Z/19 and 06Z/19 as it enters the low-level jet southeast of the low-pressure center. To represent the balance of forces affecting the accel-

eration of this parcel, the geostrophic (U_g) and ageostrophic (U_{ag}) winds are listed in Table 3. The U_g vector can be used as a measure of the magnitude and direction of the pressure gradient force. The U_{ag} vector is a measure of the imbalance between the pressure gradient and Coriolis forces. If U_{ag} is directed to the left (right) of the direction of the total wind (U), there is an instantaneous acceleration (deceleration) of the parcel. Between 03Z/19 and 06Z/19, the magnitude of U_g ($|U_g|$) increases significantly as the parcel accelerates toward the storm center. Since the vertical motion during this period is weak, this change in $|U_g|$ implies that isallobaric effects associated with the large SLP tendencies (see map inset in Fig. 7e) are making an important contribution to parcel accelerations during this period.

The parcel *rapidly* accelerates during the following 3.5 h with wind speeds approaching 37 m s^{-1} and the $|U_{ag}|$ exceeding 40 m s^{-1}. Given the large changes in $|U_g|$, the isallobaric wind is still making an important contribution to the acceleration of the parcel into the LLJ. However, the vertical displacement of the parcel after 09Z/19 is also an important factor. The increase in the ascent of the parcel between 09Z/19 and 10Z/19 from −1.7 to −7.0 μb s^{-1} within an environment in which the U_g changes with height enhances the ageostrophic nature of the flow and contributes to the increase of the magnitude of $|U|$ from 30 to 37 m s^{-1} during this hour (Table 3). As the parcel enters the region of strong ascent associated with the precipitation maximum and associated latent heat release north of the surface low (as indicated by increasing θ, decreasing q, and large negative values of ω between 10Z/19 and 12Z/19 in Table 3), it moves through the 850 and 700 mb layers and to the west of the closed low aloft. At this point, the parcel trajectory is directed toward higher geopotential heights. The parcel thus decelerates and turns sharply to the right, a turn that marks the western boundary of the precipitation shield to the northwest

TABLE 3. Listing for cold conveyor belt parcel (trajectory 5 in Fig. 18b) for times listed in left-hand column. The variables include pressure (p, mb), potential temperature (θ, K), specific humidity (q, g kg^{-1}), vertical motion (ω, μb s^{-1}), wind direction ($320 = 320°$), and speed (m s^{-1}) listed for total (U), geostrophic (U$_g$), and ageostrophic (U$_{ag}$) winds. Isobaric absolute vorticity, stretching, and tilting terms as listed in Table 2.

Time	Lat	Long	p	θ	q	ω	U	U$_g$	U$_{ag}$	$\zeta_\theta + f$	$\partial\theta/\partial p$	PV	$\zeta_p + f$	Stretch	Tilt
								Direction/speed							
12Z/18	36.0	65.5	925	275.2	1.9	0.7	327/11	4/16	225/10	5.7	0.043	2.5	10.9	−0.3	0.7
00Z/19	32.8	67.3	970	280.9	5.0	0.6	88/10	124/5	60/7	4.4	0.005	0.2	4.4	−0.5	0.0
03Z/19	33.0	68.7	977	282.5	5.7	1.0	107/12	132/10 .	57/5	4.3	0.003	0.1	4.3	−0.8	0.0
06Z/19	33.7	70.3	989	284.6	6.4	0.5	126/18	171/23	41/16	1.8	0.003	0.1	1.8	−0.4	0.0
07Z/19	34.1	70.9	990	284.9	7.1	−0.1	132/20	176/23	53/17	2.3	0.009	0.2	2.3	−0.2	0.0
08Z/19	34.6	71.5	989	285.7	7.7	−0.3	134/24	175/37	35/25	2.9	0.009	0.3	2.9	−0.8	0.0
09Z/19	35.3	72.4	986	286.9	8.5	−1.7	133/30	186/47	46/37	2.7	0.016	0.4	2.7	−0.6	0.0
10Z/19	36.1	73.3	973	288.9	9.5	−7.0	147/37	248/25	117/48	6.0	0.042	2.5	6.0	10.1	0.0
11Z/19	37.3	73.8	923	289.9	8.1	−21.2	173/34	258/31	128/44	28.2	0.052	14.8	28.3	71.7	0.2
12Z/19	38.3	74.0	778	294.4	5.0	−68.6	159/26	144/33	285/11	57.0	0.037	·21.2	59.4	143.6	−6.8
18Z/19	41.1	73.6	381	302.8	0.1	−2.3	269/11	13/5 .	247/13	15.4	0.014	2.2	14.5	−6.5	0.5

of the simulated storm system, as indicated by the sharp gradients along the western edge of relative humidity maximum depicted in Fig. 6a. This pattern is consistent with Eliassen and Kleinschmidt's (1957, pp. 132–137) description of the flow through a deepening cyclone and with Carlson's (1980) schematic of the relationship of the cold conveyor belt to the precipitation and cloud distribution to the north and west of an extratropical cyclone.

The vorticity diagnostics listed in Table 3 indicate that the cold conveyor belt is marked by a rapid increase in both the PV and absolute vorticity. The changes in PV are associated with the latent heat release, as will be discussed for parcel 6. The increase in the absolute vorticity is due primarily to an order of magnitude increase in the stretching term between 10Z/19 and 12Z/19. The stretching increases as the parcel begins to decelerate and rapidly rise through the 850 to 700 mb layer. As the parcel rises above 700 mb into the region of maximum mass divergence aloft (Fig. 7g)

after 1215Z/19, the stretching term decreases to −6.5 × 10^{-9} s^{-2} and the absolute vorticity decreases, coinciding with the anticyclonic turn of the trajectory toward the east over New Jersey and Long Island (Fig. 18).

d. Warm conveyor belt

Parcel 6 in Fig. 18b and Table 4 is chosen to represent the parcels which approach the developing cyclone from the south. These parcels begin at a higher pressure with higher values of θ and q than those in the cold conveyor belt discussed earlier. Between 09Z/19 and 11Z/19, the parcel is accelerating toward the developing storm system in response to the isallobaric wind (in association with the increasing gradients in the SLP field) and also to the increasing ascent in a region where the geostrophic wind (i.e., the pressure gradient force) is changing with height. By 1130Z/19, the speed exceeds 31 m s^{-1} as the parcel ascends to 798 mb just east of the developing surface low (Fig. 18b).

TABLE 4. Listing for warm conveyor belt parcel (trajectory 6 in Fig. 18b) for times listed in left-hand column. Column headings and units are listed in Tables 2 and 3.

Time	Lat	Long	p	θ	q	ω	U	U$_g$	U$_{ag}$	$\zeta_\theta + f$	$\partial\theta/\partial p$	PV	$\zeta_p + f$	Stretch	Tilt
								Direction/speed							
12Z/18	29.6	72.9	1025	283.0	8.4	−0.2	99/6	108/18	293/12	7.3	0.037	2.7	7.3	0.3	0.0
00Z/19	31.1	77.5	1019	290.3	9.6	−0.4	162/18	232/11	127/18	5.4	0.033	1.7	5.4	0.8	0.0
06Z/19	34.3	76.3	1001	289.8	11.1	−1.8	224/17	350/11	203/26	25.6	0.035	8.8	25.7	19.6	−0.1
09Z/19	35.6	74.9	960	289.4	9.3	−6.8	211/18	280/20	152/22	36.7	0.041	15.0	37.5	50.8	−1.7
10Z/19	36.3	74.5	923	290.2	8.3	−13.3	203/22	257/28	126/23	37.4	0.069	25.8	37.2	59.6	3.1
1030Z/19	36.6	74.3	894	291.3	7.6	−18.9	198/25	250/34	115/27	32.4	0.032	10.3	36.8	57.3	−15.8
11Z/19	37.1	74.2	854	292.5	6.7	−24.9	192/28	243/37	112/29	38.8	0.037	14.3	38.4	60.6	−8.1
1130Z/19	37.6	74.1	798	294.2	5.5	−38.9	187/31	224/30	117/19	49.6	0.032	15.9	47.1	66.8	22.9
12Z/19	38.1	74.0	706	297.1	3.9	−64.0	184/28	165/27	263/9	59.7	0.033	19.8	59.7	13.5	59.4
13Z/19	39.0	74.0	482	303.7	0.7	−42.6	180/27	213/40	74/23	27.6	0.026	7.3	27.5	−71.2	−0.2
14Z/19	39.9	73.9	403	304.6	0.2	−9.6	193/27	146/6	203/23	16.2	0.019	3.1	12.6	−9.1	−7.7
15Z/19	40.7	73.5	379	304.4	0.2	−4.8	213/23	93/8	227/27	18.8	0.015	2.8	9.4	−1.9	−4.9
18Z/19	41.7	70.9	336	304.2	0.1	−1.8	263/23	298/7	250/18	13.3	0.020	2.6	2.6	−1.6	−4.5

Sechrist and Dutton (1970) emphasize the importance of the rapid acceleration of parcels approaching a coastal cyclone from the south and east (in conjunction with the increasing gradients in the SLP) and show that these accelerations are an important source of kinetic energy for the entire storm budget.

As was the case for parcels in the cold conveyor belt and dry airstream, the parcels in the warm conveyor belt are marked by a concurrent increase in the potential vorticity and isobaric absolute vorticity between 09Z/19 and 12Z/19 (Table 4). The increase in the absolute vorticity is due primarily to the stretching below 700 mb. As the parcel ascends above the 700 mb level, it passes through the region of maximum mass divergence (Fig. 7h) and associated negative stretching (or vortex compression), resulting in a decrease in absolute vorticity after 12Z/19. The parcel turns anticyclonically during this period and is directed northeastward and then eastward off the New England coast by 21Z/19 (Fig. 18b).

The increase in PV to values greater than 10×10^{-6} K mb^{-1} s^{-1} between 06Z/19 and 12Z/19 occurs as this parcel passes through the low-level PV maximum diagnosed within the coastal front/inverted trough (Section 4c). The increase of the PV *following a parcel* is related to diabatic processes through the expression

$$\frac{d(PV)}{dt} = -(\zeta_\theta + f)\frac{\partial\dot\theta}{\partial p} + \frac{\partial\theta}{\partial p}\left[\mathbf{k}\cdot\left(\nabla_\theta\dot\theta \times \frac{\partial\mathbf{V}}{\partial\theta}\right)\right], \quad (4)$$

which neglects friction. An evaluation of the first term in Eq. (4) for parcel 6 (Fig. 18b) between 1130Z/19 and 12Z/19 and the second term (transformed to p space) for the 2° × 2° box surrounding the storm center on the 700 mb level at 12Z/19 (Fig. 16d) indicates that the first term is approximately one order of magnitude larger than the second term and accounts for nearly 70% of the PV increase diagnosed with respect to parcel 6. Although there are difficulties in making comparisons between these two terms, it appears from these results that the vertical gradients in $\dot\theta$ related to the latent heating profiles in the region of precipitation near and above the inverted trough/coastal front is an important contributing factor to the development and maintenance of the low-level PV maximum for the model simulation, a result which is consistent with Boyle and Bosart (1986). The θ profile (which is increasing with increasing θ within the 1000 to 600 mb layer) yields a net transport of mass from lower isentropic layers to the adjacent layers above, increasing the stability in the lower troposphere and thus contributing to the increase of the PV in the lower troposphere. Finally, the decrease of PV following the parcels as they rise rapidly through the middle troposphere north and east of the storm center (Tables 2–4) is consistent with the profile of $\dot\theta$ above the level of maximum latent heat release.

e. Summary of the trajectory computations

As is the case for other cyclones [e.g., see Young et al. (1987)], the rapid cyclogenesis is related to the interaction of several well-defined airstreams which converge into the rapidly developing low-level circulation after 09Z/19. A dry airstream, consisting of dry, high PV air, originates within a tropopause fold over the northern plains and descends into the storm system from the west-southwest. A cold conveyor belt, consisting of cold, moist air, originates in a region of subsidence within the cold anticyclone off the Northeast Coast and approaches the storm from the east-southeast. A warm conveyor belt, consisting of warm, moist air, originates in the PBL to the south of the storm system and accelerates through the storm system. As parcels converge into the developing storm, they pass through the PV maximum confined to the lower troposphere along the coast, with the PV increase experienced by the parcel related primarily to the vertical distribution of $\dot\theta$. Absolute vorticity is increased below 700 mb primarily through stretching associated with the convergence of these airstreams. After experiencing intense stretching, parcels rise rapidly through the low-level ascent maximum north and east of the storm system, advecting large values of absolute vorticity upward and contributing to the extension of the vortex from the lower toward the middle troposphere. After converging toward the ascent maximum, the warm and cold conveyor belts and dry airstream parcels diverge as they rise and turn anticyclonically north and east of the surface low. The divergence of these airstreams to the north and east of the surface low contributes to the mass divergence above 700 mb and the associated rapid deepening of the storm, as measured by the decreasing SLP.

It appears that the convergence of airstreams in a simulated mid-latitude cyclone is similar, at least qualitatively, to that diagnosed for a simulated, intense mesoscale convective system by Rotunno and Klemp (1985). They use a similar trajectory approach to analyze the circulation around a material curve which surrounds the maximum of low-level vertical vorticity in a simulated meso-low associated with a supercell thunderstorm. They found that air just to the east of the vorticity maximum originates at low levels and ascends as it approaches the storm center. The air to the west is relatively colder and drier, originating aloft and descending toward the storm center. Both streams are drawn together in the low-level updraft. In addition, Rotunno and Klemp found that parcels approaching the storm encounter weak positive tilting followed by intense stretching, allowing the vertical vorticity created by tilting to be increased exponentially as the parcels enter the low-level updraft. Although the spatial and temporal scales of a meso-low associated with a supercell thunderstorm and the Presidents' Day cyclone

are quite different, processes associated with the convergence of air descending from the middle to upper troposphere and air ascending from the lower troposphere appear to contribute to the rapid spinup of both systems.

7. Summary and conclusions

A diagnostic analysis based on a regional-scale model simulation of the rapid development phase of the Presidents' Day cyclone on 19 February 1979 is presented to complement and extend the previous diagnostic analyses which were based on the observational data base. Data from the numerical model is used to investigate the structure and evolution of a tropopause fold beneath the axis of an intensifying polar jet upwind of the region of incipient cyclogenesis. An indirect transverse circulation beneath the jet core, which concentrates the subsidence on the warm side of the upper-level front, contributes to the intensifying frontal zone in the middle and upper troposphere and the descent of dry stratospheric air marked by high values of potential vorticity (PV). The path of this descending stratospheric air follows the PJ-trough system eastward to a position just west of the developing surface system by 09Z/19, as inferred by Uccellini et al. (1985) using radiosonde and TOMS ozone data. By 12Z/19, the descending PV maximum becomes superimposed over a low-level PV maximum associated with the developing coastal front/inverted trough aligned along the Carolina and Virginia coasts. The rapid development phase of the Presidents' Day cyclone coincides with the arrival of this dry, stratospheric air mass in the cyclogenetic region and its eventual superposition over

the low-level PV maximum. The model results show that the stratospheric extrusion down toward the 700 mb level can be associated with jet-streak and associated frontogenetical processes and occurs well before and upstream of the cyclogenetic event. These results point to a more active role for the subsynoptic-scale processes associated with jet streaks and fronts in the total evolution of the storm in contrast to the concept that these processes are a passive consequence of the cyclogenetic process, an issue discussed by Palmén and Newton (1969, p. 585) and more recently highlighted by Keyser and Shapiro (1986, p. 493).

The model simulation of the interaction between two separate PV maxima is consistent with the conceptual model described by Hoskins et al. (1985), which is reproduced in Fig. 19. Through an "invertibility principle" first expressed by Kleinschmidt (1950), Hoskins et al. show that a positive PV anomaly that extends downward from the stratosphere into the middle troposphere acts to induce a cyclonic circulation which extends *throughout the entire troposphere to the earth's surface* (Fig. 19a). Furthermore, a positive PV anomaly associated with a low-level baroclinic region will also induce a cyclonic circulation extending upward throughout the entire troposphere (Fig. 19b). This circulation can add to the circulation induced from the upper-level system, as long as the low-level anomaly remains downwind of the upper-level anomaly, maintaining a positive feedback between the two systems. This scenario discussed by Hoskins et al. (1985) from a potential vorticity perspective is similar to the "type B" cyclogenesis described by Petterssen and Smebye (1971) which involves the advection of absolute vor-
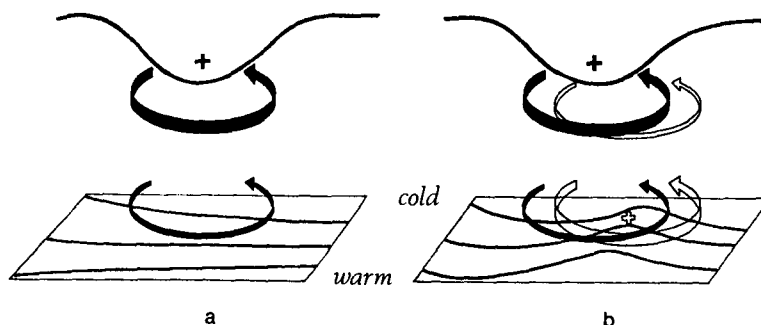

FIG. 19. A schematic picture of cyclogenesis from Hoskins et al. (1985) associated with the arrival of an upper air PV anomaly over a low-level baroclinic region. In (a), the upper air cyclonic PV anomaly, indicated by a solid plus sign and associated with the low tropopause shown, has just arrived over a region of significant low-level baroclinicity. The circulation induced by the anomaly is indicated by solid arrows, and potential temperature contours are shown on the ground. The advection by this circulation leads to a warm temperature anomaly somewhat ahead of the upper PV anomaly as indicated in (b), and is marked with an open plus sign. This warm anomaly induces the cyclonic circulation indicated by the open arrows in (b) that acts to reinforce the circulation pattern induced by the upper air PV anomaly.

ticity ahead of an upper-level trough that overtakes a low-level baroclinic zone.

The Eulerian and Lagrangian model diagnostics reveal the following: 1) Cold, dry air which originates in the lower stratosphere and upper troposphere within the tropopause fold over the north-central United States descends toward the storm center from the southwest. At the same time, air which originates at low levels within a strong surface high located to the north of the developing storm is moistened and warmed as it flows within the ocean-influenced PBL toward the storm system and then ascends and accelerates as it approaches the storm center from the east and southeast. These two airstreams correspond to the dry airstream and the cold conveyor belt in Carlson's (1980) conceptual model of airflow through mid-latitude cyclones. The convergence of these airstreams coincides with the rapid spinup of the storm system and is responsible for the asymmetric cloud distribution observed in the satellite imagery for this case. 2) A warm conveyor belt is also diagnosed for this simulated cyclone. The southerly current accelerates toward the surface low from the south-southwest, passes through the low-level PV maximum, ascends through the storm system, and then turns toward the northeast. 3) The vertical absolute vorticity of parcels in all of the airstreams is increased primarily by intense vertical stretching below the 700 mb level in the region where the various airstreams appear to converge. The concentration of vorticity by convergence (stretching) dominates in the lower troposphere with the vertical and horizontal vorticity advections acting to increase the vorticity in the middle troposphere. 4) The ascent and divergence of the airstreams north and northeast of the developing storm center are associated with a mass divergence maximum located near 500 mb (with the level of nondivergence located near 700 mb) that contributes to the continual deepening and propagation of the simulated surface low.

These model results indicate that the convergence of various airstreams, which originate at distances ranging up to 2000 km away from the storm center and undergo important changes during the 24 h prior to cyclogenesis, played a crucial role in the rapid spinup of the storm system. The convergence allowed for the realization of the high potential for a spinup represented by the separate PV maxima in the upper and lower troposphere. Furthermore, the subsequent divergence of the airstreams just to the north and east of the surface low is related to the increasing mass divergence above 700 mb, which contributes to the rapid deepening of the surface cyclone as measured by the decreasing SLP. Given the interaction among the various physical processes throughout the entire troposphere and lower stratosphere, attempts to isolate the relative importance of upper- and lower-tropospheric processes that combine to produce rapidly developing cyclones are likely not very meaningful, especially since these processes

appear to interact in a mutually beneficial manner as they contribute to the rapid cyclogenesis.

Finally, the issue concerning the accuracy of this numerical simulation of the Presidents' Day cyclone and whether the diagnostics presented here are more representative of the model simulation (with all of its weaknesses) than the actual storm still remains. The uncertainty involving the accuracy of the deepening rate of the simulated cyclone after 12Z/19 compared to Bosart's (1981) analyses raises legitimate concerns as to whether the model is properly accounting for the ocean-influenced PBL, the grid-resolvable precipitation, and the possible influence of subgrid-scale convection during this period not only on the deepening rates, but also on the magnitude of ω diagnosed near the storm center. Our initial model-based diagnostic study (Whitaker 1986) used a different 36-h simulation which was marked by different precipitation and deepening rates after 12Z/19. Despite these differences, the trajectory computations, the potential and absolute vorticity diagnostics, and mass divergence fields were very similar to those presented in this paper. This favorable comparison would seem to provide supporting evidence for the ability of the regional-scale model output to complement and extend *synoptic studies* as discussed by Keyser and Uccellini (1987). However, the sensitivity of numerical models to differences in the treatment of the various physical processes and the apparent inability of many of these models to capture the period of most rapid deepening associated with oceanic cyclones suggest that the means by which mesoscale processes contribute to explosive cyclogenesis are still not properly simulated by the models. The level of uncertainty points to the continued requirements for 1) improving physical parameterization schemes in the models and 2) conducting additional model-based diagnostic studies for a large variety of storms, both of which will depend on 3) more detailed observations of the oceanic storms. It is anticipated that future field experiments such as the Experiment on Rapidly Intensifying Cyclones over the Atlantic (ERICA) will lead to an increased understanding of the interaction of physical and dynamical processes that lead to explosive cyclogenesis and will increase our ability to numerically simulate and predict these storms.

TIME							
TRJ #		12Z/18	18Z/18	00Z/19	06Z/19	12Z/19	18Z/19	00Z/20

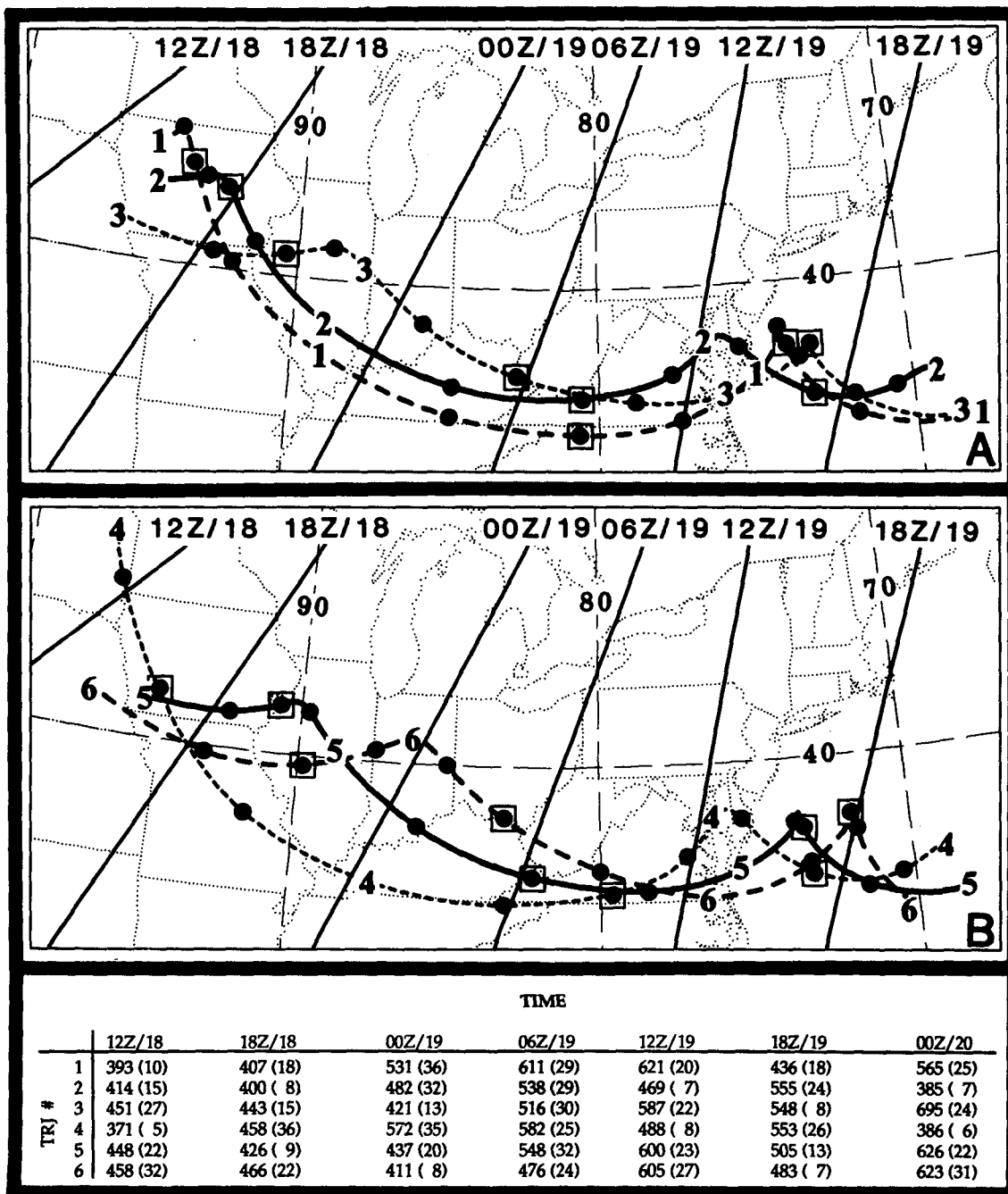| TRJ #		12Z/18	18Z/18	00Z/19	06Z/19	12Z/19	18Z/19	00Z/20
	1	393 (10)	407 (18)	531 (36)	611 (29)	621 (20)	436 (18)	565 (25)
	2	414 (15)	400 (8)	482 (32)	538 (29)	469 (7)	555 (24)	385 (7)
	3	451 (27)	443 (15)	421 (13)	516 (30)	587 (22)	548 (8)	695 (24)
	4	371 (5)	458 (36)	572 (35)	582 (25)	488 (8)	553 (26)	386 (6)
	5	448 (22)	426 (9)	437 (20)	548 (32)	600 (23)	505 (13)	626 (22)
	6	458 (32)	466 (22)	411 (8)	476 (24)	605 (27)	483 (7)	623 (31)

FIG. 20. A collection of six 36-h middle-tropospheric trajectories computed forward from 1200 UTC 18 February. Trajectory numbers (1–6, bold) are placed at 12-h intervals along the trajectory. Large dots mark 3-h positions. Values of pressure (mb) and wind speed (m s⁻¹, in parentheses) are given in the table for each parcel trajectory numbered 1 through 6 for positions marked by numbers or dots enclosed by a box (6-h interval). Solid lines in a and b denote position of trough axes for the time indicated.

APPENDIX

Cyclic Nature of Parcel Trajectories in the Dry Airstream

In section 6, parcel trajectories are utilized to isolate a dry airstream directed from the tropopause fold region toward the southwest quadrant of the developing cyclone. This airstream appears to flow directly from the upper troposphere over the north-central United States to the low to middle troposphere over the East Coast. However, another set of parcel trajectories was isolated within this dry airstream that displays an oscillatory characteristic as shown in Figs. 20a and 20b. These parcels appear to be confined to a layer between 400 and 650 mb and pass through several cycles as they approach the trough axis that is propagating from west to east at an average rate of 24 m s^{-1}. When these parcels are located to the west of the trough axis, they descend and accelerate toward the southeast and attain velocities greater than the propagation rate of the trough axis. Given this increasing velocity, these parcels eventually move to the east of the trough axis, rise to pressure levels near (or less than) 500 mb, turn toward the northeast, and decelerate to velocities that are less than the propagation rate of the trough. Thus, the trough axis catches up to and passes the decelerating parcel, which again becomes located within the confluent region west of the trough axis, where the cycle is repeated. From these results, it would appear that the dry airstream represents a complex interaction of parcel trajectories that either descend directly through the baroclinic zone below 700 mb before accelerating through the storm system or continually oscillate within the middle troposphere, interacting with the trough/PJ in a cyclic manner as the entire system propagates from west to east.

REFERENCES

Anthes, R. A., and D. Keyser, 1979: Tests of a fine-mesh model over Europe and the United States. *Mon. Wea. Rev.*, **107**, 963–984.

Bjerknes, J., and J. Holmboe, 1944: On the theory of cyclones. *J. Meteor.*, **1**, 1–22.

Bleck, R., 1973: Numerical forecasting experiments based on the conservation of potential vorticity on isentropic surfaces. *J. Appl. Meteor.*, **12**, 737–752.

——, and C. Mattocks, 1984: A preliminary analysis of the role of potential vorticity in Alpine lee cyclogenesis. *Beitr. Phys. Atmos.*, **57**, 357–368.

Bosart, L. F., 1981: The Presidents' Day snowstorm of 18–19 February 1979: A subsynoptic-scale event. *Mon. Wea. Rev.*, **109**, 1542–1566.

——, and S. C. Lin, 1984: A diagnostic analysis of the Presidents' Day storm of February 1979. *Mon. Wea. Rev.*, **112**, 2148–2177.

Boyle, J. S., and L. F. Bosart, 1986: Cyclone-anticyclone couplets over North America. Part II: Analysis of a major cyclone event over the eastern United States. *Mon. Wea. Rev.*, **114**, 2432–2465.

Browning, K. A., 1971: Radar measurements of air motion near fronts. *Weather*, **26**, 320–340.

——, and T. W. Harrold, 1969: Air motion and precipitation growth in a wave depression. *Quart. J. Roy. Meteor. Soc.*, **95**, 288–309.

Businger, J. A., 1973: Turbulent transfer in the atmospheric surface layer. *Workshop on Micrometeorology*, D. A. Haugen, Ed., Amer. Meteor. Soc., 392 pp.

Carlson, T. N., 1980: Airflow through midlatitude cyclones. *Mon. Wea. Rev.*, **108**, 1498–1509.

Carr, F. H., and J. P. Millard, 1985: A composite study of comma clouds and their association with severe weather over the Great Plains. *Mon. Wea. Rev.*, **113**, 370–387.

Danielsen, E. F., 1968: Stratospheric–tropospheric exchange based upon radioactivity, ozone and potential vorticity. *J. Atmos. Sci.*, **25**, 502–518.

——, 1974: The relationship between severe weather, major dust storms and large scale cyclogenesis (II). *Subsynoptic Extratropical Weather Systems: Observations, Analysis and Prediction. Notes from a Colloquium: Summer 1974*, Vol. 11, NCAR Rep. No. ASP-C0-3-V-2, 226–241 [NTIS PB247286].

——, 1980: Stratospheric source for unexpectedly large values of ozone measured over the Pacific Ocean during GAMETAG, August, 1977. *J. Geophys. Res.*, **85**, 401–412.

Eliassen, A., and E. Kleinschmidt, 1957: Dynamical meteorology. *Handbuch der Physik*, Vol. 48, J. Bartles, Ed., Springer-Verlag, 1–154.

Gyakum, J. R., 1983: On the evolution of the *QE II* storm. II: Dynamic and thermodynamic structure. *Mon. Wea. Rev.*, **111**, 1156–1173.

Hoskins, B. J., M. E. McIntyre and A. W. Robertson, 1985: On the use and significance of isentropic potential vorticity maps. *Quart. J. Roy. Meteor. Soc.*, **111**, 877–946.

Johnson, D. R., and W. K. Downey, 1975: The absolute angular momentum of storms: Quasi-Lagrangian diagnostics 2. *Mon. Wea. Rev.*, **103**, 1063–1076.

——, and ——, 1976: The absolute angular momentum budget of an extratropical cyclone: Quasi-Lagrangian diagnostics 3. *Mon. Wea. Rev.*, **104**, 3–14.

Kaplan, M. L., J. W. Zack, V. C. Wong and J. J. Tuccillo, 1982: Initial results from a mesoscale atmospheric simulation system and comparisons with the AVE–SESAME I data set. *Mon. Wea. Rev.*, **110**, 1564–1590.

Keyser, D., and M. A. Shapiro, 1986: A review of the structure and dynamics of upper-level frontal zones. *Mon. Wea. Rev.*, **114**, 452–499.

——, and L. W. Uccellini, 1987: Regional models: Emerging research tools for synoptic meteorologists. *Bull. Amer. Meteor. Soc.*, **68**, 306–320.

Kleinschmidt, E., 1950: On the structure and origin of cyclones (Part 1). *Meteor. Rundsch.*, **3**, 1–6.

Koch, S. E., W. C. Skillman, P. J. Kocin, P. J. Wetzel, K. F. Brill, D. A. Keyser and M. C. McCumber, 1985: Synoptic scale forecast skill and systematic errors in the MASS 2.0 model. *Mon. Wea. Rev.*, **113**, 1714–1737.

Krishnamurti, T. N., 1968: A study of a developing wave cyclone. *Mon. Wea. Rev.*, **96**, 208–217.

Molinari, J., 1982: A method for calculating effects of deep cumulus convection in numerical models. *Mon. Wea. Rev.*, **110**, 1527–1534.

Newton, C. W., 1956: Mechanisms of circulation change during lee cyclogenesis. *J. Meteor.*, **13**, 528–539.

Palmén, E., and C. W. Newton, 1969: *Atmospheric Circulation Systems, Their Structure and Physical Interpretation. Geophys. Res.*, Vol. 13, Academic Press, 603 pp.

Petterssen, S., and S. J. Smebye, 1971: On the development of extratropical storms. *Quart. J. Roy. Meteor. Soc.*, **97**, 457–482.

Reed, R. J., 1955: A study of a characteristic type of upper-level frontogenesis. *J. Meteor.*, **12**, 226–237.

——, and E. F. Danielsen, 1959: Fronts in the vicinity of the tropopause. *Arch. Meteor. Geophys. Bioklim.*, **A11**, 1–17.

Rotunno, R., and J. B. Klemp, 1985: On the rotation and propagation

of simulated supercell thunderstorms. *J. Atmos. Sci.,* **42,** 271–292.

Sechrist, F. S., and J. A. Dutton, 1970: Energy conversions in a developing cyclone. *Mon. Wea. Rev.,* **98,** 354–362.

Shapiro, M. A., 1970: On the applicability of the geostrophic approximation to upper-level frontal motions. *J. Atmos. Sci.,* **27,** 408–420.

——, 1975: Simulation of upper-level frontogenesis with a 20-level isentropic coordinate primitive equation model. *Mon. Wea. Rev.,* **104,** 591–604.

——, L. S. Fedor and T. Hampel, 1987: Research aircraft measurements of a polar low over the Norwegian Sea. *Tellus,* **39A,** No. 4, 272–306.

Stage, S. A., and J. A. Businger, 1981: A model for entrainment into a cloud-topped marine boundary layer. Part I: Model description and application to a cold air outbreak episode. *J. Atmos. Sci.,* **38,** 2213–2229.

Uccellini, L. W., P. J. Kocin, R. A. Petersen, C. H. Wash and K. F. Brill, 1984: The Presidents' Day cyclone of 18–19 February 1979: Synoptic overview and analysis of the subtropical jet streak influencing the pre-cyclogenetic period. *Mon. Wea. Rev.,* **112,** 31–55.

——, D. Keyser, K. F. Brill and C. H. Wash, 1985: The Presidents' Day cyclone of 18–19 February 1979: Influence of upstream trough amplification and associated tropopause folding on rapid cyclogenesis. *Mon. Wea. Rev.,* **113,** 962–987.

——, R. A. Petersen, K. F. Brill, P. J. Kocin and J. J. Tuccillo, 1987: Synergistic interactions between an upper-level jet streak and diabatic processes that influence the development of a low-level jet and a secondary coastal cyclone. *Mon. Wea. Rev.,* **115,** 2227–2261.

Whitaker, J. S., 1986: A diagnostic study of explosive oceanic cyclogenesis using a mesoscale model simulation. M.S. thesis, Department of Meteorology, Florida State University, Tallahassee, FL 32306–3034, 83 pp.

Young, M. V., G. A. Monk and K. A. Browning, 1987: Interpretation of satellite imagery of a rapidly deepening cyclone. *Quart. J. Roy. Meteor. Soc.,* **113,** 1089–1115.